

Quasi-full-visible-light absorption by D35-TiO₂/g-C₃N₄ for synergistic persulfate activation towards efficient photodegradation of micropollutants

Lei Yang, Xue Bai, Juan Shi, Xinyu Du, Lu Xu, Pengkang Jin*

Key Laboratory of Northwest Water Resources, Environment and Ecology, Ministry of Education, School of Environmental and Municipal Engineering, Xi'an University of Architecture and Technology, Xi'an, Shaanxi Province, 710055, China



ARTICLE INFO

Keywords:
g-C₃N₄TiO₂dye-sensitization
Persulfate
Visible-light photodegradation
g-C₃N₄
TiO₂
Dye-sensitization
Persulfate
Visible-light photodegradation

ABSTRACT

To utilize the excellent charge separation efficiency of the g-C₃N₄/TiO₂ photocatalyst and broaden its narrow visible-light absorption range, D35 dye-sensitization was employed to synthesize a novel D35-TiO₂/g-C₃N₄ photocatalyst. Due to the complementary co-absorption ability of g-C₃N₄ and the D35 dye, the D35-TiO₂/g-C₃N₄ nano-composite exhibits a quasi-full-visible-light harvesting range up to 675 nm, and the simultaneous electron injection from the D35 and g-C₃N₄ to TiO₂ synergistically activates persulfate (PS) to produce the active oxidizing species more efficiently. In the D35-TiO₂/g-C₃N₄/PS photocatalytic system, 10 mg/L bis-phenol A (100 mL) could be completely removed in only 15 min with 0.5 g/L photocatalyst and 2 mM PS under visible-light illumination ($\lambda > 400$ nm); meanwhile, nearly 50% of BPA was mineralized into nontoxic substances. Radical quenching experiments and electron paramagnetic resonance (EPR) spectra revealed that 'OH, SO₄²⁻, 'O₂⁻ and h⁺ all contributed to organics elimination, and the radical process was the main degradation pathway. The efficient photodegradation of other typical micropollutants, such as caffeine, phenol, acetaminophen and methylene blue, indicating that the D35-TiO₂/g-C₃N₄/PS photocatalytic system has a strong non-selective oxidative ability to remove micropollutants. Therefore, it has great potential to be applied in water environment remediation.

1. Introduction

Conventional advanced oxidation processes (AOPs) such as ozone oxidation, photo-Fenton technology and photocatalysis are all efficient methods for refractory contaminant degradation [1–3]. In recent years, AOPs based on the sulfate radical (SO₄²⁻) have gained wide interest in research [4]. Compared to the hydroxyl radical ('OH), the sulfate radical has a higher redox potential (2.5–3.1 V), longer half-life time, higher selectivity and adaptability to a wide pH range [5,6]. Sulfate radicals can be produced by activation of persulfate (PS) or peroxymonosulfate (PMS) [4,7]. There are various activation methods, such as heat, alkali, radiation, transition-metal ions and metal oxides activation, as well as carbonaceous-based materials activation [8–14]. Among these techniques, carbonaceous-based materials activation is more cost-effective and eco-friendly.

Graphitic carbon nitride (g-C₃N₄) is a polymeric layered material, with a structure similar to graphene [15]. The optical absorption boundary of g-C₃N₄ is located at approximately 450 nm; therefore, it has visible-light absorption ability. Many studies focused on g-C₃N₄ photocatalysis which have been applied in environmental remediation

[16–18]. However, only a few studies have paid attention to PS or PMS activation by g-C₃N₄ photocatalysis. Liu et al. enhanced BPA degradation in a g-C₃N₄/PS visible-light photocatalytic system [19]. Feng et al. synthesized the Fe-g-C₃N₄ catalyst through introducing Fe element into g-C₃N₄, which could activate PMS to degrade phenol with sunlight [20]. Kim et al. thermally transformed urea into g-C₃N₄, and it was employed to simultaneously remove azo dye and As (III) from solution with the addition of PS [21]. However, the fast recombination of charge carriers still limits the application of g-C₃N₄ photocatalysis. Combining g-C₃N₄ with nano-TiO₂ has been proven to be an efficient method by which to enhance the electron-hole pairs separation due to their appropriate energy level difference [22,23]. Until now, the activation performance of TiO₂/g-C₃N₄ heterojunction towards persulfate has seldom been studied.

The band gap of pristine TiO₂ is 3.2 eV, so it can only absorb ultraviolet light ($\lambda < 390$ nm) [24–28]. In TiO₂/g-C₃N₄, TiO₂ merely plays a role in accepting the excited electrons from the g-C₃N₄ conduction band (CB) under visible-light illumination. To improve the visible-light harvesting efficiency, we employed dye-sensitization to anchor the visible-light-absorbing dye molecules onto the unoccupied

* Corresponding author.

E-mail addresses: pkjin@hotmail.com, pkjin@xauat.edu.cn (P. Jin).

TiO₂ surface of TiO₂/g-C₃N₄. Dye sensitization has been proven to be a successful technique for broadening the light absorption of TiO₂ into the visible light region, exhibiting promising performance in the photocatalytic degradation of contaminants [25–29]. Therefore, sensitizer is significantly crucial for dye-sensitized photocatalysis, affecting the light harvesting efficiency and stability of the photocatalysts. Various dye sensitizers can be categorized into three main classes, i.e., xanthene dyes (e.g., eosin Y, rhodamine B, erythrosine), transition-metal-based dyes (e.g., Ru (II), Ir (III) complexes) and organic dyes (e.g., porphyrins, phthalocyanines) [30]. Although the xanthene dyes have wide visible-light absorption range and low cost, the photo-conversion efficiencies and chemical stabilities are relatively low [31]. The sensitized photocatalysts with transition-metal-based dyes possess higher photocatalytic activity and stability, however, the high cost of synthesis and potential toxicity of transition-metal ions limit their practical application [32]. In contrast, without the above shortcomings, organic dyes are widely used in dye-sensitized photocatalysis, especially porphyrin and phthalocyanine dyes [33]. The organic dye coded as D35, which is synthesized by Sun and Hagfeldt, exhibits outstanding photovoltaic performance in dye-sensitized solar cells (DSCs) [31]. It shows a considerably high light-harvesting efficiency due to the wide visible-light absorption range (400–675 nm) and the high extinction coefficient. Moreover, the unique molecular structure of D35 leads to highly efficient electron injection into TiO₂ and the effective suppression of charge recombination [34–36]. Additionally, the low cost of synthesis, stable physico-chemical properties and negligible toxicity make D35 dye a cost-effective, eco-friendly and sustainable material used in the dye-sensitization process. Although its application in DSCs has been widely reported, the D35-sensitized photocatalyst had never been studied before we first employed the D35-TiO₂ nano-crystalline film in a wastewater treatment process [29].

In this study, we constructed a photocatalytic system featuring with the complementary co-absorption of visible light and synergistic activation of persulfate. The wide visible-light absorption of D35 dye fitly complements the absorption of TiO₂/g-C₃N₄ leading to almost full-visible-spectrum light absorption by the D35-TiO₂/g-C₃N₄ photocatalyst. Moreover, the energy level of conduction band edge (E_{CB}) of g-C₃N₄ (~ -1.17 eV) and the lowest unoccupied molecular orbital (LUMO) level of D35 dye (~ -1.37 eV) are both more negative (higher) than the E_{CB} of TiO₂ (~ -0.31 eV) [36–38]. In theory, there will be a sufficient driving force of Gibbs free energy for both the D35 sensitizer and the g-C₃N₄ to inject photo-induced electrons into the TiO₂ conduction band [39]. Then, the injected electrons will synergistically activate persulfate to produce a large quantity of reactive oxidizing species for pollutant degradation. To characterize the photocatalysts, SEM, TEM, XRD, FT-IR, TGA, UV-vis DRS, PL, time-resolved PL and XPS were employed. We chose *bis*-phenol A (BPA) as the target pollutant to evaluate the photocatalytic performance of the D35-TiO₂/g-C₃N₄/PS system. Experiments were performed under different degradation conditions (i.e., BPA concentration, pH, catalyst dosage, PS dosage and D35 dye concentration) to find the optimum environment for BPA degradation. The stability and reaction selectivity of the D35-TiO₂/g-C₃N₄/PS photocatalytic system were also investigated. Moreover, the reactive oxidizing species were explored to support the proposed reaction mechanism and BPA degradation pathways.

2. Experiments

2.1. Materials

Analytical-grade tetrabutyl titanate, isopropanol, hydrofluoric acid and acetonitrile (Macklin, China), D35 dye (Dyedamo, Sweden) were purchased for photocatalyst preparation. Al₂O₃, BPA (purity 99.9%), potassium peroxydisulfate, NaOH, HCl, methanol, *tert*-butyl-alcohol, 1,4-benzoquinone, EDTA-2Na, methylene blue, caffeine, acetaminophen and phenol were procured from Aladdin (China). Spin trap

5, 5-dimethyl-1-pyrroline-N-oxide (DMPO, Macklin, China), and chromatographic-grade methanol and acetonitrile (Fisher Scientific, USA) were purchased for EPR and HPLC analysis. All chemicals were used as received. Ultrapure water (18.25 MΩ cm) was used for all synthesis and treatment processes.

2.2. Preparation of the photocatalysts

Carbon nitride (g-C₃N₄) was synthesized by heating melamine powder. First, 10 g of melamine was placed into an alumina crucible with a cover and heated in a muffle furnace at 550 °C for 3 h with a heating rate of 2.5 °C/min. After cooling to room temperature, the resultant powders were collected. A certain amount of the as-prepared g-C₃N₄, 6.8 g of tetrabutyl titanate and 50 mL of isopropanol constituted the mixture suspension, and was treated by ultrasonic dispersion for 30 min. Then, 1.5 mL of hydrofluoric acid (40 wt.%) was added into the above suspension with magnetic stirring for 10 min. Next, the mixture suspension was sealed into a Teflon-lined autoclave at 180 °C for 12 h. The synthesized TiO₂/g-C₃N₄ hybrids were washed several times by high-speed centrifugation, and then dried at 80 °C for 5 h, subsequently ground into powder with a mortar. For the dye-sensitization process, 17.84 μM D35 dye solution in acetonitrile was prepared. Then, 1 g of the resultant TiO₂/g-C₃N₄ powder was dispersed in 50 mL of the D35 dye solution stirring for 10 h to achieve a high surface coverage, and then dried in an oven at 60 °C. For brevity, we name the 5%, 10%, 20%, 30%, 40% and 50% g-C₃N₄ weight-ratio of TiO₂/g-C₃N₄ samples as TCN_{0.05}, TCN_{0.1}, TCN_{0.2}, TCN_{0.3}, TCN_{0.4} and TCN_{0.5}, respectively. Moreover, after the D35 dye-sensitization process, the resultant samples are called DTCN, e.g., DTCN_{0.3}. In addition, D35-Al₂O₃ nano-composite was employed in PL and time-resolved PL measurements as a comparison. The preparation method was similar to the dye-sensitization process of TCN samples where TCN was substituted by Al₂O₃.

2.3. Experimental setup and BPA removal process

The performance of the as-synthesized D35-TiO₂/g-C₃N₄ photocatalyst in PS activation was evaluated by BPA degradation. The catalytic procedure was performed in a 250 mL customized double-walled high-borosilicate glass beaker with a cooling water recirculation system (WG-DCX, Shanghai Instrument Physical Optics Instrument Co., Ltd., China) to maintain the constant reaction temperature at 22 °C. A 300 W Xe lamp with a 400 nm cut-off filter (CEL-HXF300, Beijing China Education Au-light Co., Ltd., China) acted as the visible light source, and the average light intensity was determined to be 105 mW/cm². In each run, 0.05 g of the D35-TiO₂/g-C₃N₄ photocatalyst was dispersed in 100 mL 10 mg/L BPA solution, and the pH was controlled at approximately 7 using 0.1 M HCl or NaOH. The suspension was continuously stirred throughout the whole reaction procedure. A 30-minute dark adsorption experiment was performed before illumination, to achieve an adsorption-desorption equilibrium between the BPA molecules and the photocatalysts, and then 2 mM PS was added into the suspension. During the experiment, 1 mL of the reaction solution was withdrawn at a certain time interval, and was then filtered through a 0.45 μm filter and prepared for HPLC analysis.

2.4. Characterization of photocatalysts

The crystal phases of the photocatalysts were characterized by a Bruker D8 Advance X-ray diffractometer (XRD) with Cu Kα radiation. The surface morphology and microstructure were observed using a Zeiss GeminiSEM500 scanning electron microscope (SEM) and a JEOL JEM-F200 transmission electron microscope (TEM) respectively. Fourier-transform infrared (FT-IR) spectra were recorded from a KBr disk on the Nicolet X700 analyzer. Thermogravimetric analysis (TGA) was performed by a Mettler Toledo TGA/DSC³⁺ analyzer. Absorption spectra were recorded on a Hitachi U3900 UV-vis spectrophotometer

(UV-vis DRS) with an integrating sphere using BaSO_4 as a reference. The chemical compositions and valence band of the photocatalysts were detected by X-ray photoelectron spectroscopy (XPS) measurements in a PHI Quantum 2000 XPS system. Photoluminescence spectroscopy (PL) and time-resolved photoluminescence spectroscopy were recorded on an Edinburgh FLS9 fluorescence spectrometer. Zeta potential of the photocatalyst was investigated by a Malvern Zetasizer Nano ZS90 analyzer.

2.5. Chemical analysis and substances identification

The degradation of organic pollutants was monitored by a high performance liquid chromatography (HPLC, Shimadzu LC-2010AHT, Japan) with a 250 mm \times 4.6 mm Hypersil BDS C18 5 μm column (Elite, China). For BPA, the mobile phase was consisted of acetonitrile and ultrapure water, with a volume ratio of 60:40 and the flow rate of 1 mL/min. A diode array detector with a detection wavelength of 278 nm was used. For caffeine, acetaminophen and phenol, the mobile phase was a mixture of methanol and ultrapure water with volume ratios of 30:70, 30:70 and 60:40, respectively, at a flow rate of 1 mL/min. The detection wavelength was 273 nm, 243 nm and 270 nm for each pollutant, respectively. The temperature of the column compartment was 30 °C. Methylene blue was detected by an UV-vis absorption spectrophotometer (TU-1901, Beijing Purkinje General Instruments Co., Ltd., China) at 664 nm. The mineralization level of BPA was detected by a total organic carbon analyzer (TOC, Shimadzu TOC-VCPh, Japan).

The intermediate products were analyzed by LCMS-IT-TOF (Shimadzu, Japan). To protect the instrument, the samples were desalting by solid-phase extraction (SPE). The method referred to *Barbara Darsinou* [40], and we used the Supelclean ENVI-18 SPE tube (3 mL, Supelco, USA). To separate the intermediates, we employed a 250 mm \times 2.0 mm Shim-pack VP-ODS C18 column (Shimadzu, Japan). The mixture of methanol and ultrapure water was used as the mobile phase and the following HPLC method was adopted: 2/98 ($\text{V}_{\text{MeOH}}/\text{V}_{\text{water}}$) for 4 min to 5/95 in 2 min; 5/95 for 3 min to 80/20 in 10 min; 80/20 for 20 min to 2/98 in 6 min; 2/98 for 8 min and then stopped. The flow rate was 0.2 mL/min, and the column temperature was maintained at 40 °C. Mass spectrographic analysis was performed in negative ion mode with an electrospray ionization source (EIS).

An electron paramagnetic resonance spectrometer (EPR, Bruker ZMXmicro-6/1, Germany) was employed to further confirm the reactive oxidizing species.

3. Results and discussion

3.1. Photocatalysts characterization

3.1.1. SEM and TEM

The morphology and microstructure of the as-prepared photocatalysts were investigated by SEM and TEM. As shown in Fig. 1a, the hydrothermally synthesized TiO_2 nanoparticles have average dimensions of 20–52 nm. In Fig. 1b, we can observe aggregated, chunky and layered $\text{g-C}_3\text{N}_4$ with a large surface area. After the hydrothermal process, TiO_2 crystals grow on the surface of the $\text{g-C}_3\text{N}_4$, which is attributed to the tetrabutyl titanate soaking into the layer of $\text{g-C}_3\text{N}_4$ (Fig. 1c). The TiO_2 distributed on the $\text{g-C}_3\text{N}_4$ decreases the particle aggregation relative to that of pristine TiO_2 . This enlarges the exposed surface area of TiO_2 and enhances the contact between the TiO_2 and the $\text{g-C}_3\text{N}_4$ components, which benefits the electron injection from $\text{g-C}_3\text{N}_4$ to TiO_2 [41]. After dye-sensitization, D35 molecules anchor onto the TiO_2 surface via $-\text{COOH}$ forming bidentate chemical bonds; therefore, the SEM image becomes slightly blurry due to the presence of the D35 layer (Fig. 1d) [29].

Fig. 2 exhibits the TEM and HRTEM-observed microstructure of the as-synthesized samples. As shown in Fig. 2a, the dimensions of the cubic TiO_2 are 20–56 nm, which is consistent with the SEM results.

Apparently, the HRTEM image in Fig. 2a displays distinct lattice fringe regions, and the average distance of the lattice spacing is 0.35 nm, which is assigned to the (101) plane of anatase TiO_2 . $\text{g-C}_3\text{N}_4$ shows a bulk layered structure (Fig. 2b), and TiO_2 is well-dispersed on the surface of $\text{g-C}_3\text{N}_4$ (Fig. 2c), which inhibits the aggregation of TiO_2 particles. In addition, the D35 dye-sensitization process can not influence the microstructure of the $\text{TiO}_2/\text{g-C}_3\text{N}_4$ samples (Fig. 2d), as we reported previously [29].

3.1.2. XRD

XRD measurements were employed to investigate the crystal phases of the pristine TiO_2 , $\text{g-C}_3\text{N}_4$, TCN and DTCN samples. As shown in Fig. 3a, the diffraction peaks of as-prepared TiO_2 at $2\theta = 25.3^\circ$, 37.8° , 48.0° , 53.9° , 55.1° , 62.7° and 70.3° respectively correspond to the (101), (004), (200), (105), (211), (204) and (116) crystal planes, which are well indexed as anatase TiO_2 (JCPDS 21-2172). The characteristic diffraction peaks at 13.2° and 27.6° can be observed in pure $\text{g-C}_3\text{N}_4$. The peak located at 13.2° corresponds to the (100) plane of $\text{g-C}_3\text{N}_4$, which is attributed to the in-plane repeated tri-s-triazine units of $\text{g-C}_3\text{N}_4$. The peak appeared at 27.6° corresponds to the (002) plane of $\text{g-C}_3\text{N}_4$, which is attributed to the stacks of the conjugated aromatic system [42,43]. It can be clearly seen that the diffraction peaks of TiO_2 and $\text{g-C}_3\text{N}_4$ are all detected in the series of the TCN samples. In terms of morphology, the SEM and TEM figures indicate that the TiO_2 crystal grows on the surface of the bulk $\text{g-C}_3\text{N}_4$. And in terms of crystal structure, the XRD patterns confirm that all the TCN samples consist of TiO_2 and $\text{g-C}_3\text{N}_4$. Thus, the SEM and TEM figures in association with the XRD patterns verify the successful synthesis of the $\text{TiO}_2/\text{g-C}_3\text{N}_4$ heterojunction. Moreover, the intensity of 27.6° diffraction peak of the as-prepared $\text{TiO}_2/\text{g-C}_3\text{N}_4$ photocatalysts gradually increase from $\text{TCN}_{0.05}$ to $\text{TCN}_{0.5}$, which suggests that the content of $\text{g-C}_3\text{N}_4$ gradually rises in these TCN samples, as we expected. It is worth noticing that the XRD diffraction peaks of $\text{DTCN}_{0.3}$ are similar to those of $\text{TCN}_{0.3}$, which indicates that the dye-sensitization process only modifies the surface, without changing the crystal structure of the TCN nanocomposites.

3.1.3. FT-IR

In order to investigate the structure of the as-synthesized nanocomposites, FT-IR analysis was employed. As shown in Fig. 3b, for TiO_2 , the broad absorption peak at $400\text{--}800\text{ cm}^{-1}$ is attributed to $\text{Ti}-\text{O}-\text{Ti}$ stretching vibrational modes [42]. In addition, the peaks around 1633 cm^{-1} and 3416 cm^{-1} are assigned to $\text{O}-\text{H}$ bending and stretching vibrations [44]. These signals may be attributed to the hydroxyl groups or water molecules adsorbed onto TiO_2 . For pure $\text{g-C}_3\text{N}_4$, three characteristic peaks can be observed. The broad absorption peak around $3000\text{--}3600\text{ cm}^{-1}$ corresponds to $\text{N}-\text{H}$ stretching vibration, and the bands between $1240\text{--}1638\text{ cm}^{-1}$ are ascribed to the typical stretching vibrations of $\text{C}-\text{N}$ and $\text{C}=\text{N}$. Additionally, the sharper peak at 812 cm^{-1} is attributed to the characteristic bending modes of the triazine ring [42,45,46]. The typical absorption peaks of pure TiO_2 and $\text{g-C}_3\text{N}_4$ all exist in the $\text{TCN}_{0.3}$ sample, which further indicates the successful synthesis of the $\text{TiO}_2/\text{g-C}_3\text{N}_4$ hybrid compound. Moreover, the FT-IR spectra of the D35 dye and $\text{DTCN}_{0.3}$ sample are also displayed. For the D35 dye, the peak located at 2873 cm^{-1} is attributed to $\text{C}-\text{H}$ symmetric stretching, and the peak at 1720 cm^{-1} corresponds to $\text{C}=\text{O}$ vibration of the carbonyl group. The peak at 1607 cm^{-1} is assigned to $\text{C}-\text{C}$ stretching vibration in the phenyl rings, and the deformation vibration of the phenyl rings is related to the peak located at 1470 cm^{-1} [47]. The four aforementioned bands correspond to the major functional groups constituting the molecular skeleton of the D35 dye (Fig. S1). The carboxyl group of the D35 dye is linked to the TiO_2 surface via a bidentate chemical bond with Ti(IV) [33,48]. All the characteristic peaks of $\text{TCN}_{0.3}$ can be found in the FT-IR spectra of $\text{DTCN}_{0.3}$. Additionally, a small peak located at 1740 cm^{-1} is also observed, corresponding to $\text{C}=\text{O}$ vibration of the carbonyl group in the spectra of the D35 dye. However, $\text{C}=\text{O}$ stretching band of the $\text{DTCN}_{0.3}$ is located at a higher

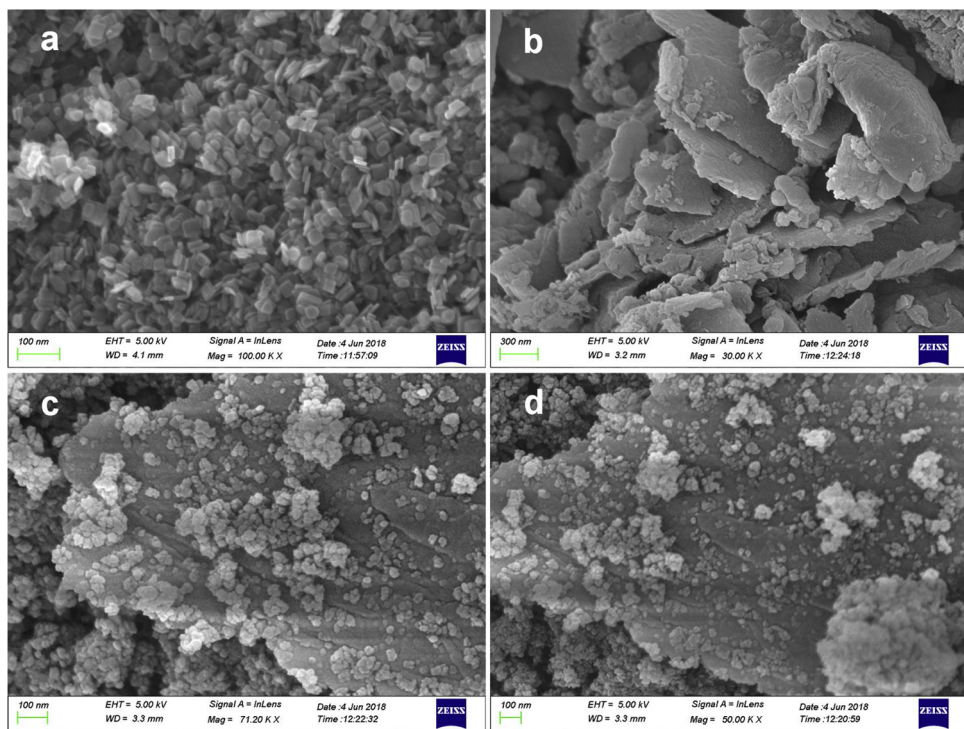


Fig. 1. SEM images of (a) TiO_2 , (b) $\text{g-C}_3\text{N}_4$, (c) $\text{TCN}_{0.3}$ and (d) $\text{DTCN}_{0.3}$ samples.

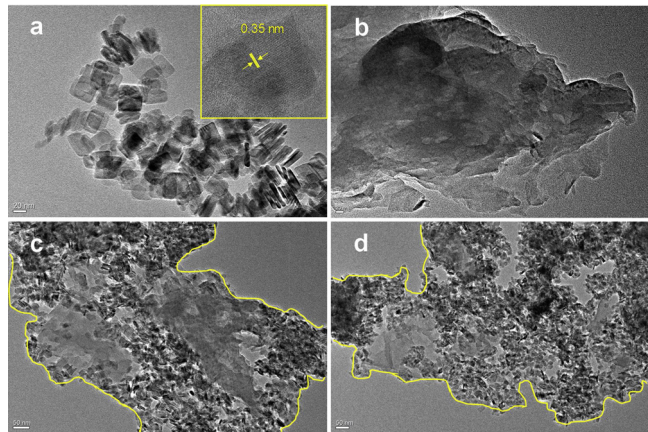


Fig. 2. TEM and HRTEM images of (a) TiO_2 , (b) $\text{g-C}_3\text{N}_4$, (c) $\text{TCN}_{0.3}$ and (d) $\text{DTCN}_{0.3}$ samples.

wavenumber than that of the D35 dye (1720 cm^{-1}). The shift might be caused by the formation of an ester-like linkage between the D35 molecule and the TiO_2 component of $\text{TCN}_{0.3}$. The bidentate chemical bond formed with Ti(IV) results in electron localization towards the O atom; thus, the signal of the $\text{C}=\text{O}$ bond shifts to a higher wavenumber [49,50]. The above results indicate successful bonding between D35 and $\text{TCN}_{0.3}$.

3.1.4. TGA

TGA was employed to investigate the thermal stability and actual content of $\text{g-C}_3\text{N}_4$ in the series of TCN photocatalysts. As displayed in Fig. 3c, the weight of pure $\text{g-C}_3\text{N}_4$ decreases from 520°C to 750°C . However, the TCN composites lose their weight within the 300°C – 600°C temperature range. The weight loss is due to $\text{g-C}_3\text{N}_4$ decomposition, and the thermal stability of the TCN composites is lower than that of pure $\text{g-C}_3\text{N}_4$, which may be attributed to that the TiO_2 nanoparticles distributed on the $\text{g-C}_3\text{N}_4$ surface lowers the π - π stacking force between the $\text{g-C}_3\text{N}_4$ layers [51–53]. The actual content of $\text{g-C}_3\text{N}_4$ in the

TCN samples is calculated according to the final weight loss of the composites. As a result, the $\text{g-C}_3\text{N}_4$ contents in the $\text{TCN}_{0.05}$ to $\text{TCN}_{0.5}$ samples are determined as 13, 30, 48, 59, 67 and 70% in weight percentage. The increased $\text{g-C}_3\text{N}_4$ content in the TCN composites is consistent with the XRD results. In contrast, the D35 dye starts to lose weight at approximately 250°C , which may be attributed to the decomposition of organic residues formed through the dye synthesis route. At 300°C , the dye itself begins to decompose, and rapid pyrolysis occurs as the temperature increases from 400°C to 610°C . According to the variation tendency of the $\text{DTCN}_{0.3}$ weight, the weight lost from 260 – 350°C is mainly due to D35 dye decomposition and the slight damaging of $\text{g-C}_3\text{N}_4$. After the dye-sensitization process, the $-\text{COOH}$ of the D35 dye anchors onto the TiO_2 surface via a bidentate chemical bond, which somewhat lowers the thermostability of the dye. When the temperature exceeds 350°C , the residual D35 dye and part of the $\text{g-C}_3\text{N}_4$ are under pyrolysis. The $\text{g-C}_3\text{N}_4$ completely decomposes with only dry TiO_2 left when the temperature further increases above 520°C . Fortunately, the thermostability of $\text{DTCN}_{0.3}$ still highly qualifies the compound for use, as photocatalysis generally takes place at room temperature.

3.1.5. UV-vis diffuse reflection and VB-XPS

The optical absorption of the pristine TiO_2 , pure $\text{g-C}_3\text{N}_4$, series of TCN and $\text{DTCN}_{0.3}$ composites was assessed by diffuse reflectance spectroscopy (DRS), as shown in Fig. 3d. The light absorption boundary of pristine TiO_2 is 390 nm , while that of pure $\text{g-C}_3\text{N}_4$ is located at 450 nm . Compared to pristine TiO_2 , the light absorption of the TCN samples shows a redshift near 450 nm , which indicates that the $\text{TiO}_2/\text{g-C}_3\text{N}_4$ composite is able to harvest visible light. After sensitizing the $\text{TCN}_{0.3}$ composite with D35 dye, a strong peak from 450 nm to 675 nm appears, which further broadens its light absorption range. Thus, the complementary light absorption of the TCN and D35 dye components leads to a wide visible-light absorption range for the DTCN photocatalysts.

The band gap energy of these photocatalysts can be calculated by the equation $E_g = 1240/\lambda_g$ (λ_g - absorption boundary of the catalyst) [54]. As a result, the band gap energies of pristine TiO_2 , pure $\text{g-C}_3\text{N}_4$,

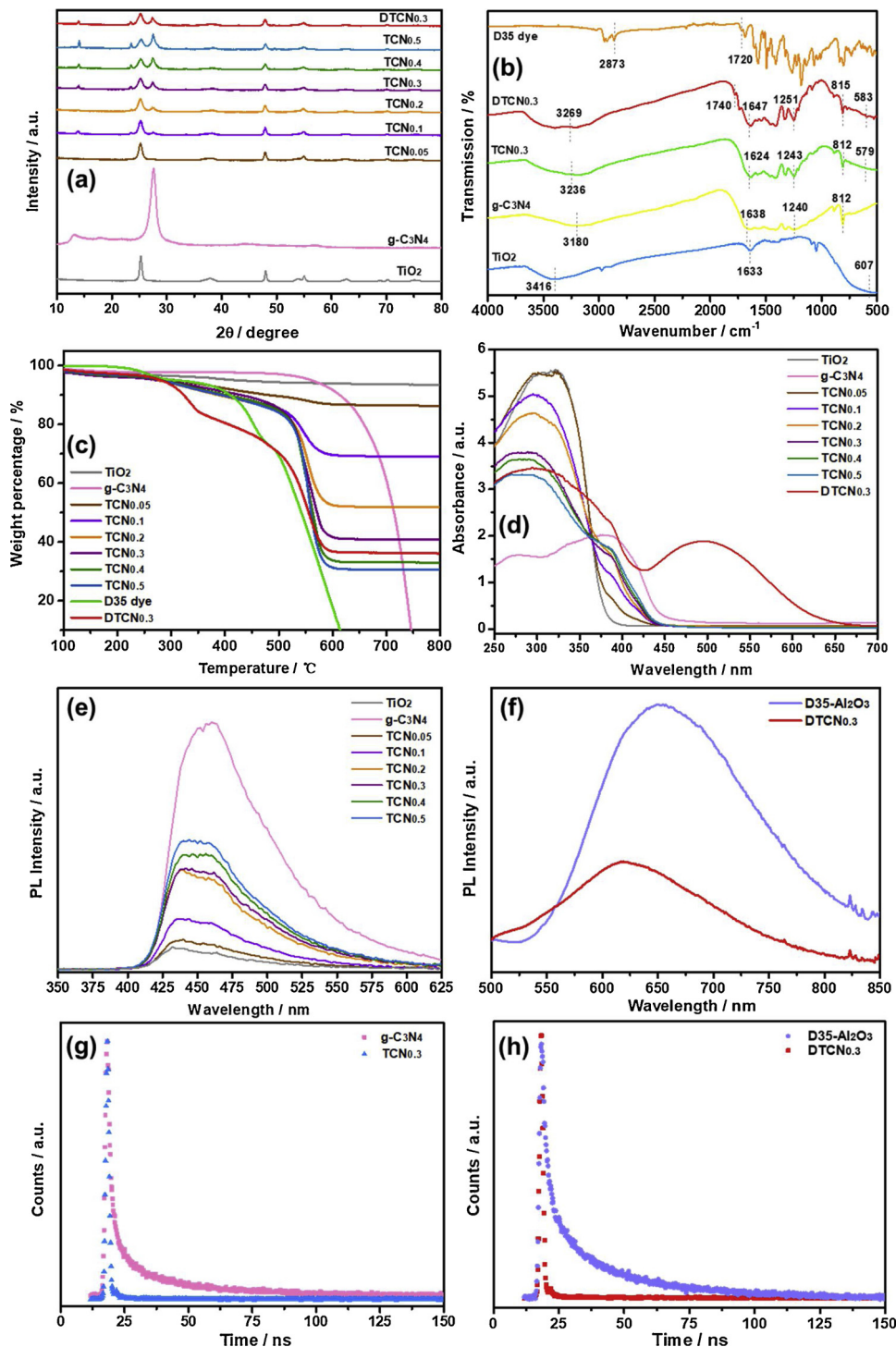


Fig. 3. Characterization of the as-prepared TiO_2 , $\text{g-C}_3\text{N}_4$, series of TCN and $\text{DTCN}_{0.3}$ samples: (a) XRD, (b) FT-IR, (c) TGA, (d) UV-vis, (e) PL spectra of TCN samples, (f) PL spectra of $\text{DTCN}_{0.3}$ and $\text{D35-Al}_2\text{O}_3$ samples, (g) time-resolved PL spectra of $\text{TCN}_{0.3}$ and $\text{g-C}_3\text{N}_4$ samples, and (h) time-resolved PL spectra of $\text{DTCN}_{0.3}$ and $\text{D35-Al}_2\text{O}_3$ samples.

$\text{TCN}_{0.05}$, $\text{TCN}_{0.1}$, $\text{TCN}_{0.2}$, $\text{TCN}_{0.3}$, $\text{TCN}_{0.4}$ and $\text{TCN}_{0.5}$ are 3.18, 2.69, 3.14, 3.05, 2.90, 2.81, 2.79 and 2.78 eV, respectively. The various values are attributed to the different contents of $\text{g-C}_3\text{N}_4$ in the TCN samples. Because dye-sensitization is a surface modification process used for semiconductors without changing their microstructure [29], the band gap energy of $\text{DTCN}_{0.3}$ is similar to that of $\text{TCN}_{0.3}$, i.e., 2.81 eV.

To further investigate the band structure of the $\text{DTCN}_{0.3}$ nanocomposite, the locations of the valence band (VB) and the conduction

band (CB) of TiO_2 and $\text{g-C}_3\text{N}_4$ were determined by UV-vis DRS and VB-XPS. As shown in Fig. S2, the VB edge of pristine TiO_2 is nearly 2.43 eV below the Fermi energy. Combined with its band gap energy of 3.18 eV, its CB edge is located at -0.75 eV (vs. NHE). For pure $\text{g-C}_3\text{N}_4$, the VB edge occurs at 1.79 eV, and its band gap energy is approximately 2.69 eV. Thus, its CB edge occurs at -0.9 eV (vs. NHE). Because of the appropriate energy level difference between pure TiO_2 and $\text{g-C}_3\text{N}_4$, there is a sufficient Gibbs free energy to induce the spontaneous electron injection from $\text{g-C}_3\text{N}_4$ CB into TiO_2 CB, which is beneficial for

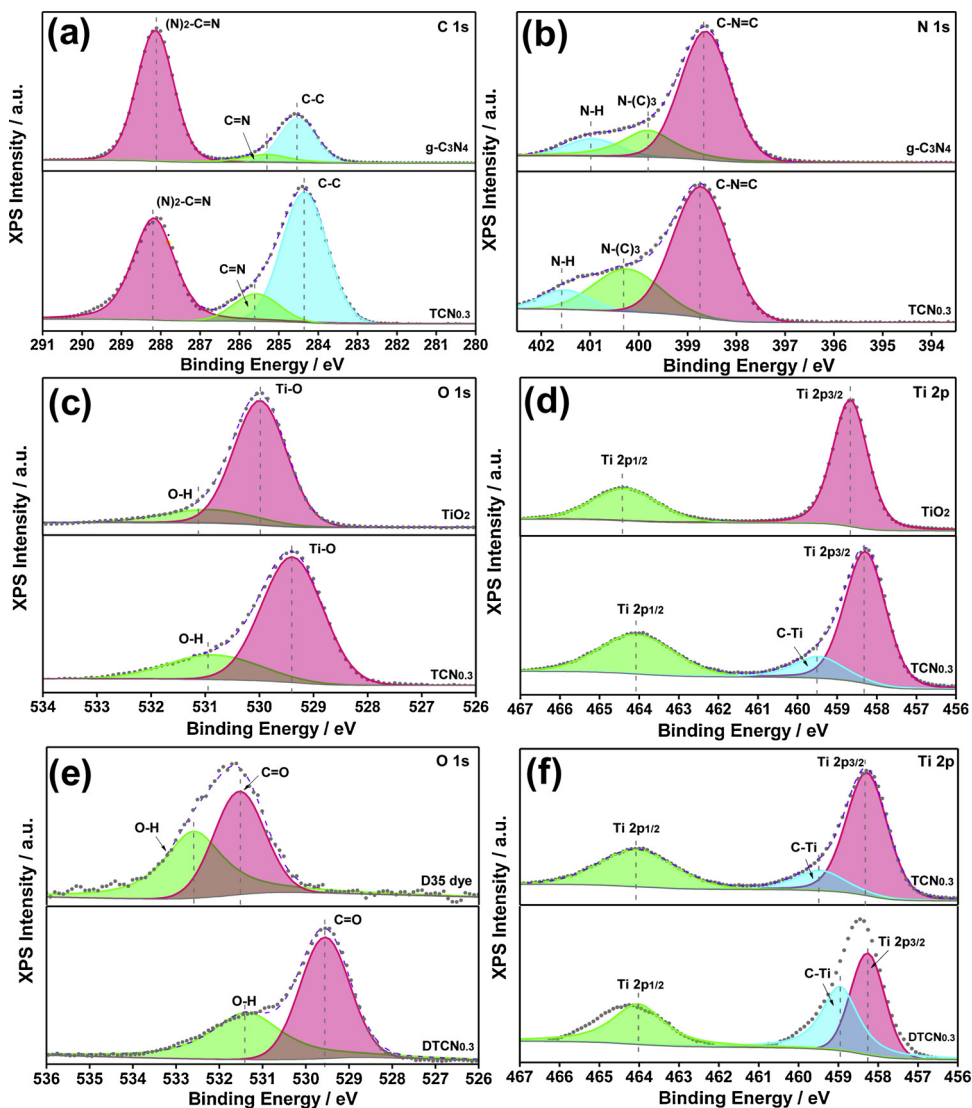


Fig. 4. C 1s, N 1s, O 1s and Ti 2p XPS spectra of TiO_2 , $\text{g-C}_3\text{N}_4$, $\text{TCN}_{0.3}$, $\text{DTCN}_{0.3}$ and D35 dye samples. The grey dots represent the original XPS data, and the purple curves are the fitting results. (For interpretation of the references to colour in this figure legend, the reader is referred to the web version of this article).

electron-hole pairs separation [39]. Moreover, as reported by Sun [36], the highest occupied molecular orbital (HOMO) of D35 dye is determined at 1.04 eV and its lowest unoccupied molecular orbital (LUMO) occurs at -1.37 eV. When the D35 dye sensitizers anchor onto the TiO_2 surface, the photo-excited electrons in the D35 LUMO can be readily injected into the TiO_2 CB [48]. Therefore, for the $\text{DTCN}_{0.3}$ photocatalyst, TiO_2 acts as an electron-acceptor, receiving excited free electrons from both D35 and $\text{g-C}_3\text{N}_4$. Then, the large quantity of electrons take part in the subsequent PS activation process.

3.1.6. PL and time-resolved PL spectral analysis

Photoluminescence spectroscopy was performed to reveal the separation efficiency of the photogenerated electron-hole pairs. $\text{DTCN}_{0.3}$ was synthesized by anchoring D35 dye onto the TiO_2 component of $\text{TCN}_{0.3}$. Both the D35 and $\text{g-C}_3\text{N}_4$ components in $\text{DTCN}_{0.3}$ can inject electrons into the TiO_2 conduction band upon visible-light excitation; however, they absorb and emit at totally different wavelengths. Therefore, we believe that it is necessary to interpret the charge separation from $\text{g-C}_3\text{N}_4$ and D35 to TiO_2 , respectively. The PL spectra of the as-prepared TCN samples are displayed in Fig. 3e. The excitation wavelength was 400 nm. Pure $\text{g-C}_3\text{N}_4$ has a strong emission peak around 460 nm, the energy of which is approximately equal to its band

gap energy (2.69 eV) [43]. When combined with TiO_2 , the intensity of the 460 nm emission peak decreases obviously. This indicates that the charge-carrier recombination is effectively restrained, which is due to that the photo-induced electrons are transferred from $\text{g-C}_3\text{N}_4$ to TiO_2 via the interfacial heterojunction [42,43]. For the various TCN photocatalysts, the emission peak intensity at 460 nm increases as the weight ratio of $\text{g-C}_3\text{N}_4$ goes up. A higher weight ratio of $\text{g-C}_3\text{N}_4$ indicates a lower weight percentage of TiO_2 , so that there may not be sufficient TiO_2 to accept the excess electrons from $\text{g-C}_3\text{N}_4$. Therefore, the recombination of the excess amount of charge carriers leads to the high PL intensity. Additionally, for pure TiO_2 , no obvious emission peak at 460 nm is observed, which is consistent with other studies [27,54].

To investigate the electron injection from the D35 dye to TiO_2 , we employed D35- Al_2O_3 as a contrast. The LUMO level of the D35 dye is located at -1.37 eV, and the conduction band of Al_2O_3 occurs at -4.45 eV (vs. NHE) [29,55]. Apparently, the excited electrons in D35 LUMO can-not be injected into Al_2O_3 due to the adverse energy level alignment. Therefore, when we use 450 nm (close the maximum absorption wavelength of D35 dye) laser to excite the D35- Al_2O_3 sample, it shows a strong PL intensity around 650 nm (Fig. 3f). Compared to D35- Al_2O_3 , the PL intensity of $\text{DTCN}_{0.3}$ approximately 650 nm is much weaker, which is highly consistent with our previous study indicating

the efficient electron injection from the D35 dye to the TiO_2 component [29].

Moreover, time-resolved PL spectra were employed to further investigate the charge transfer in the as-prepared samples. Generally, a shorter lifetime is related to the fast separation of electron-hole pairs (electron injection takes place in the fs-ps time domain), while a longer lifetime is associated with recombination of the charge carriers (ns- μ s time domain) [56,57]. For pure $\text{g-C}_3\text{N}_4$ and the $\text{TCN}_{0.3}$ samples, we chose 400 nm as the excitation wavelength and 460 nm as the emission wavelength (Fig. 3g). After multi-exponential fitting, the calculated PL decay time constants (τ_A) are shown in Table S1. The τ_A values of pure $\text{g-C}_3\text{N}_4$ and $\text{TCN}_{0.3}$ are calculated as 1.452 ns and 0.683 ns, respectively. It can be clearly seen that the τ_A value of $\text{TCN}_{0.3}$ is much less than that of pure $\text{g-C}_3\text{N}_4$, which indicates that the charge-carrier separation becomes more efficient in $\text{TCN}_{0.3}$ after introducing TiO_2 . This further confirms the fast electron-injection from $\text{g-C}_3\text{N}_4$ CB into TiO_2 CB, which is consistent with the steady-state PL results above. For the $\text{DTCN}_{0.3}$ and $\text{D35-Al}_2\text{O}_3$ samples, 450 nm was selected as the excitation wavelength for the effective stimulation of D35 dye, and 650 nm was chosen as the emission wavelength accordingly (Fig. 3h). The τ_A values of $\text{D35-Al}_2\text{O}_3$ and $\text{DTCN}_{0.3}$ are calculated as 2.228 ns and 0.763 ns, respectively. The much smaller τ_A value of $\text{DTCN}_{0.3}$ than that of $\text{D35-Al}_2\text{O}_3$ indicates the much lesser charge recombination in $\text{DTCN}_{0.3}$, due to the effective electron injection from D35 to TiO_2 . Hence, according to the above analysis, when $\text{DTCN}_{0.3}$ is illuminated by visible light, the excited electrons in both $\text{g-C}_3\text{N}_4$ and D35 can be injected into the TiO_2 CB, leading to efficient charge-carrier separation, which benefits the subsequent persulfate activation process.

3.1.7. XPS analysis

The chemical compositions of pure TiO_2 , $\text{g-C}_3\text{N}_4$, $\text{TCN}_{0.3}$, $\text{DTCN}_{0.3}$ and D35 dye samples were investigated by X-ray photoelectron spectroscopy. Fig. 4a displays the C 1s high-resolution spectra of pure $\text{g-C}_3\text{N}_4$ and $\text{TCN}_{0.3}$ samples. For $\text{g-C}_3\text{N}_4$, the C 1s spectrum can be split into 3 different Gaussian-Lorentzian peaks centred at the binding energies of 284.52, 285.33 and 288.14 eV. The peak at approximately 284.52 eV is attributed to the C–C coordination of adventitious carbon contamination. The peaks at 285.33 eV and 288.14 are attributed to the C=N and (N)₂-C=N groups, respectively [43,58]. For $\text{TCN}_{0.3}$, its C 1s spectrum is similar to that of pure $\text{g-C}_3\text{N}_4$, but the peaks of C=N and (N)₂-C=N groups shift towards higher binding energies by 0.27 and 0.04 eV, respectively. Fig. 4b shows the N 1s high-resolution spectra of pure $\text{g-C}_3\text{N}_4$ and $\text{TCN}_{0.3}$ samples. There are three peaks in the splitting pattern in the N 1s spectrum of pure $\text{g-C}_3\text{N}_4$. The peak located around 398.63 eV is assigned to C=N=C groups. The peaks at 399.8 and 400.95 eV are attributed to N-(C)₃ and N–H groups, respectively [59]. These three peaks show small shifts of 0.1, 0.2 and 0.35 eV towards higher binding energies in the $\text{TCN}_{0.3}$ N 1s spectrum. In the O 1s spectrum of TiO_2 (Fig. 4c), two peaks can be observed. The peak around 529.9 eV is assigned to the Ti–O bond, and the peak at 531.5 eV is attributed to the O–H bond [60]. For $\text{TCN}_{0.3}$, the Ti–O peak shifts by 0.51 eV towards a lower binding energy. In the Ti 2p spectrum of TiO_2 (Fig. 4d), the two peaks located around 458.65 and 464.34 eV are attributed to Ti 2p_{3/2} and Ti 2p_{1/2}, respectively. In $\text{TCN}_{0.3}$, the two peaks shift towards lower binding energies by 0.36 and 0.28 eV, respectively. Additionally, a new peak at approximately 460.0 eV appears in the Ti 2p spectrum of $\text{TCN}_{0.3}$, which is assigned to the C–Ti bond according to previous work [44].

Compared to pure $\text{g-C}_3\text{N}_4$ and TiO_2 , the C 1s and N 1s peaks of $\text{TCN}_{0.3}$ shift towards higher binding energies; meanwhile, its O 1s and Ti 2p peaks shift to lower binding energies. The small shifts to lower binding energies for both Ti 2p_{3/2} and Ti 2p_{1/2} after hybridization of TiO_2 with $\text{g-C}_3\text{N}_4$ are probably attributed to the partial substitution of Ti–O by Ti–C or Ti–N. Since the electronegativity of the C and N elements are smaller than that of O, the electron density on Ti is enhanced, so the Ti 2p peaks shift towards lower binding energies. In contrast, the

electron densities on C and N are decreased, and both of the peaks shift to higher binding energies. This indicates that chemical bonds are formed between TiO_2 and $\text{g-C}_3\text{N}_4$ [42,43,45], and further demonstrates the successful synthesis of $\text{TiO}_2/\text{g-C}_3\text{N}_4$ heterojunction.

The O 1s spectrum can provide information on the surface structure and bonding interaction between the anchoring group of the dye and the catalyst surface (Fig. 4e). For D35, the peaks located at 531.54 eV and 532.60 eV are attributed to the C=O and COOH group respectively. For $\text{DTCN}_{0.3}$, the peak assigned to C=O of D35 appears at 529.56 eV, and the OH peak attributed to the COOH group of D35 and TiO_2 is located at 531.37 eV. Compared to pure D35, the O 1s peaks of $\text{DTCN}_{0.3}$ shift towards lower binding energies. This suggests that the chemical environment around O is changed after the dye-sensitization process, which is consistent with other reports [61,62]. The COOH of D35 anchors onto the TiO_2 component by forming a bidentate chemical bond; thus, the chemical environment of the Ti in $\text{DTCN}_{0.3}$ must be changed as well (Fig. 4f). The Ti 2p_{3/2} and Ti 2p_{1/2} peaks of $\text{DTCN}_{0.3}$ are located at 458.25 eV and 464.02 eV, and the C–Ti bond linking $\text{g-C}_3\text{N}_4$ and TiO_2 is at 458.95 eV. The Ti peaks all shift to lower binding energies compared to those of $\text{TCN}_{0.3}$ (the peaks of Ti 2p_{3/2}, Ti 2p_{1/2} and C–Ti appear at 458.29, 464.06 and 460.0 eV, respectively), which is probably due to the upward energy level shift of the TiO_2 band structure caused by the change in the surface dipole after D35-sensitization [61]. The above results collectively indicate that the $\text{D35-TiO}_2/\text{g-C}_3\text{N}_4$ photocatalyst has been successfully synthesized.

3.2. The effect of the $\text{g-C}_3\text{N}_4$ doping concentration

Fig. 5a displays the photocatalytic performance of the $\text{TiO}_2/\text{g-C}_3\text{N}_4$ catalysts with different $\text{g-C}_3\text{N}_4$ doping levels. The results indicate that pristine TiO_2 can not activate PS under visible light. The slight decline of the BPA concentration is due to the surface adsorption of the as-prepared TiO_2 nanoparticles. At the low doping concentrations of $\text{g-C}_3\text{N}_4$ ranging from 5% to 30%, the PS activation activity of $\text{TiO}_2/\text{g-C}_3\text{N}_4$ is gradually improved for higher BPA removal efficiencies. When the content of $\text{g-C}_3\text{N}_4$ is 30%, the $\text{TiO}_2/\text{g-C}_3\text{N}_4$ catalyst has the optimal photocatalytic activity for PS activation under visible light, and the BPA removal efficiency is nearly 90% within 20 min. As the doping concentration further increases to 40% and 50%, the photocatalytic activity drops.

As discussed in the PL section, a $\text{g-C}_3\text{N}_4$ weight ratio that is too high in the TCN sample may lead to an excess number of excited electrons in $\text{g-C}_3\text{N}_4$. Compared to $\text{TCN}_{0.1} \sim \text{TCN}_{0.3}$, the charge recombination of $\text{TCN}_{0.4}$ and $\text{TCN}_{0.5}$ is relatively faster, so the corresponding BPA removal efficiency is not satisfactory. However, although the charge separation efficiencies of $\text{TCN}_{0.05} \sim \text{TCN}_{0.2}$ are higher than that of $\text{TCN}_{0.3}$, the corresponding relatively low BPA degradation efficiencies are attributed to the decreased amount of visible-light harvesting with lower $\text{g-C}_3\text{N}_4$ weight ratios. Therefore, to balance the charge separation efficiency and visible-light absorption, $\text{TCN}_{0.3}$ presents relatively high performance in PS activation and BPA degradation. We finally chose $\text{TCN}_{0.3}$ for the subsequent dye-sensitization process and the following studies.

3.3. Evaluation of photocatalytic activity

The activity of the $\text{DTCN}_{0.3}$ photocatalyst was evaluated by BPA degradation under visible-light irradiation with or without PS addition. For comparison, control experiments were also performed. As shown in Fig. 5b and c, the $\text{TCN}_{0.3}/\text{PS}$ system shows a relatively high efficiency of BPA degradation at 88% within 20 min. After D35 sensitization, the $\text{DTCN}_{0.3}/\text{PS}$ system can completely degrade BPA within 15 min at the reaction rate of 0.285 min^{-1} , which is almost 3 times higher than that of the $\text{TCN}_{0.3}/\text{PS}$ system (0.099 min^{-1}). Moreover, the TOC degradation efficiency nearly reaches 50% (Fig. 5d). When the D35 sensitizers are combined with the TCN composite, the resulting large improvement

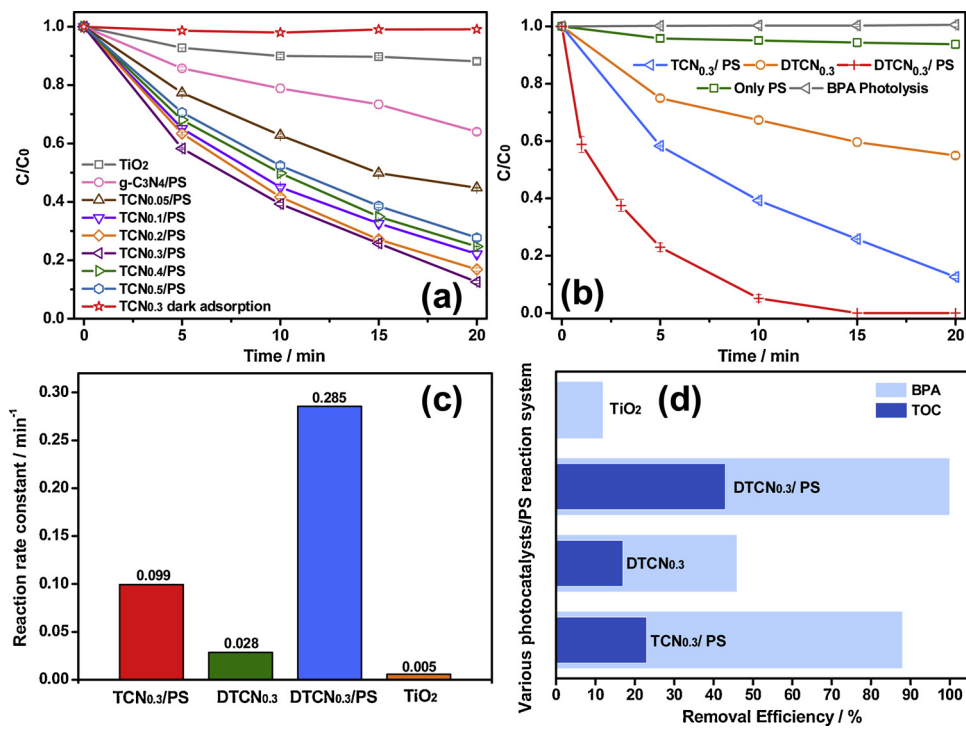


Fig. 5. (a) Effects of the g-C₃N₄ doping concentration on PS activation, (b) the BPA degradation efficiency in the DTCN_{0.3}/PS system and control experiments, (c) the BPA degradation rate constant in various photocatalytic systems, and (d) the BPA degradation and mineralization efficiency in various photocatalytic systems.

of the BPA degradation rate is attributed to the complementary co-absorption of visible light and synergistic PS activation. As depicted in the UV-vis section, the light absorption edge of TCN_{0.3} is 450 nm; meanwhile, a new absorption peak from 450 to 675 nm appears after the D35 dye is introduced. This higher visible-light harvesting efficiency will lead to more excited electrons being generated in the DTCN_{0.3} photocatalyst. Subsequently, the large quantity of free electrons can synergistically activate PS to produce a large amount of reactive oxidizing species for faster BPA degradation [63]. However, the BPA degradation efficiency is only 45%, and the TOC removal is only 16.8% for the DTCN_{0.3} photocatalyst without PS addition (Fig. 5b and d). Such results reveal that the D35 dye-sensitizer and PS are two crucial components in the highly efficient DTCN_{0.3}/PS photocatalytic system.

3.4. Effect of variable reaction parameters

3.4.1. Initial BPA concentration

To optimize the DTCN_{0.3}/PS system for BPA photodegradation, different reaction parameters were evaluated. The initial BPA concentration is an important factor influencing the degradation efficiency [64]. In this study, we set four different BPA concentrations, i.e., 5, 10, 20 and 30 mg/L. As shown in Fig. 6a, 5 mg/L BPA can be quickly degraded within 10 min, while 10 mg/L BPA needs 15 min. However, when the initial BPA concentration increases to 20 and 30 mg/L, the degradation efficiencies are only 84% and 65% within 20 min.

To study the kinetics of BPA degradation by the DTCN_{0.3}/PS photocatalytic system, the data were fitted by the deformed Langmuir-Hinshelwood model (Eq.1) [65]:

$$-\ln\left(\frac{C_t}{C_0}\right) = k_{app}t \quad (1)$$

The apparent rate constant of 5 mg/L BPA degradation reaches 0.492 min⁻¹, while those of the other three concentrations are 0.285, 0.085 and 0.052 min⁻¹, respectively. It can be clearly seen that the BPA degradation rate and efficiency decrease as the initial concentration increases, which is consistent with other reports [64,66]. When the

dosage of the photocatalyst and PS remain fixed, the quantity of the produced active sites and oxidizing species in the photocatalytic process also remain constant. As the initial BPA concentration increases to higher levels, the amount of produced reactive oxidizing species becomes less and less sufficient to degrade the contaminants, so the reaction rate decreases gradually. Therefore, we chose 10 mg/L as the model BPA concentration in this study.

3.4.2. Initial solution pH

The pH values of natural water bodies lie within a wide range. Therefore, it is important to investigate how the pH affects BPA degradation in the DTCN_{0.3}/PS system. As shown in Fig. 6b, when the initial pH ranges from 3.0 to 7.0, BPA is completely degraded within 15 min. The apparent reaction rate constant at pH 7 (0.285 min⁻¹) is slightly faster than it is at pH 3 (0.258 min⁻¹). Excluding experimental error, this result can be explained by the electrostatic interaction between BPA and the photocatalysts. Therefore, the zeta potential was measured to reveal the surface electrical properties of DTCN_{0.3} at different pH values. As shown in Fig. S3, the DTCN_{0.3} surface is positively charged at pH 3, while it becomes negatively charged at pH 5~11. Based on a previous study, the pKa value of BPA is approximately 9.6, below which BPA is positively charged and above which BPA is negatively charged [67]. At pH 3, both BPA and the DTCN_{0.3} sample are positively charged, while at pH 5 and 7, electrical properties of the two are opposite. Therefore, the Coulomb attraction of BPA and DTCN_{0.3} may lead to the slightly faster reaction rate at pH 7 than at pH 3. When the pH increases to 9.0, the reaction rate drops to 0.123 min⁻¹, and the final degradation efficiency of BPA is 93%. Although the Coulomb interaction between DTCN_{0.3} and BPA is also attractive at pH 9.0, the decrease of the BPA degradation rate is mainly because part of the SO₄²⁻ react with OH⁻, producing ·OH in basic conditions, which has a shorter lifetime and weaker oxidation potential than SO₄²⁻ [68]. When the initial solution pH further increases to 11.0, the reaction rate sharply decreases to 0.046 min⁻¹, and only 63% of the BPA is degraded. On one hand, the Coulomb repulsion between the photocatalysts and BPA molecules impedes their contact. On the other hand, the D35 dye

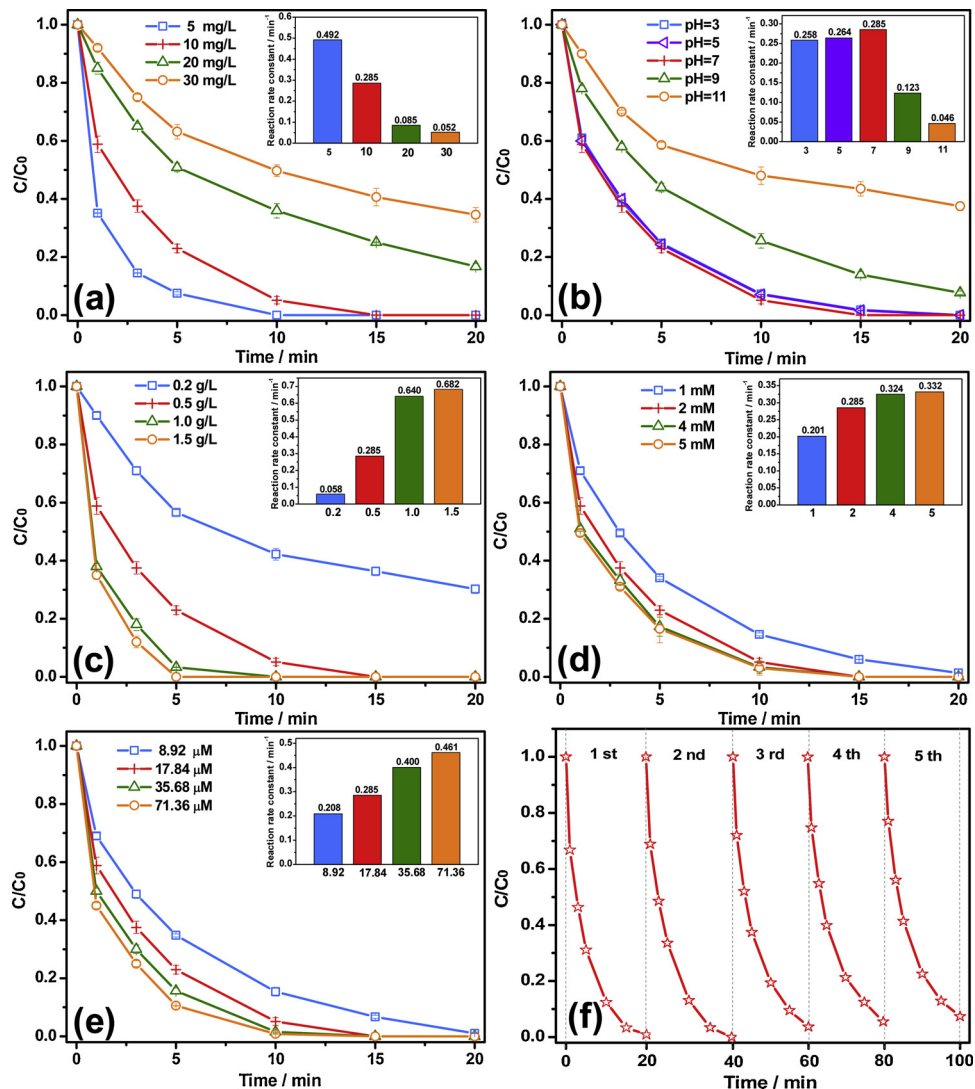


Fig. 6. The BPA degradation efficiency and rate constant in the $\text{DTCN}_{0.3}/\text{PS}$ system under various reaction conditions: (a) initial BPA concentration, (b) initial solution pH, (c) dosage of $\text{DTCN}_{0.3}$ photocatalyst, (d) initial PS concentration, and (e) D35 sensitizer concentration. (f) Cyclic utilization of the $\text{DTCN}_{0.3}$ photocatalyst for BPA degradation with PS addition.

(Photocatalyst: 50 mg; BPA: 10 mg/L, 100 mL; pH = 7; PS: 2 mM; D35 dye solution: 17.84 μM . In each experiment, only a single factor was altered, while the other parameters were fixed according to the description.)

sensitizers desorb from the photocatalysts in basic solutions [29], which weakens the visible-light absorption of the $\text{DTCN}_{0.3}$ and further affects the quantity of activated PS. We finally chose pH 7.0 as the initial solution pH.

3.4.3. Dosage of photocatalysts

We also investigated how the dosage of the $\text{DTCN}_{0.3}$ photocatalyst affected BPA degradation. We tested 4 different $\text{DTCN}_{0.3}$ dosages with the PS fixed at 2 mM. As displayed in Fig. 6c, the BPA degradation rate and efficiency increase as the dosage of the photocatalyst increases from 0.2 to 1.5 g/L. When the dosage increases to 0.5 g/L or more, BPA can be completely degraded within 15 or 10 min. As the dosage of the photocatalyst increases, many more incident photons can be harvested by $\text{DTCN}_{0.3}$ to generate a large quantity of free electrons, so that more PS can be activated. With more reactive sites on the photocatalysts and the produced oxidizing species, the organic contaminants can be rapidly removed. However, when the dosage of the photocatalyst increases up to 1.5 g/L, the reaction rate barely increases compared to the rate at 1.0 g/L. This may be attributed to the limited quantity of PS. Thus, to further increase the reaction rate, more PS needs to be

supplemented into the reaction system to provide more reactive oxidizing species. To balance the efficiency and economy, we chose 0.5 g/L as the optimum photocatalyst dosage in the subsequent experiments.

3.4.4. Dosage of PS

Apart from the dosage of the photocatalyst, the quantity of PS is also a crucial parameter in this photocatalytic system. The dosage of PS was varied from 1 to 5 mM with the $\text{DTCN}_{0.3}$ concentration fixed at 0.5 g/L. As shown in Fig. 6d, when 1 mM PS is added into the reaction system, the BPA degradation efficiency reaches 100% within 20 min, and its degradation rate constant is 0.201 min^{-1} . As we expected, the BPA degradation efficiency increases as the PS dosage goes up. The reaction rate constant with 2 mM PS (0.285 min^{-1}) is faster than that with 1 mM PS, and BPA can be completely eliminated within 15 min. However, no significant promotion of BPA removal can be observed upon further increasing PS concentration from 4 to 5 mM. This may be attributed to the following two reasons: (1) at higher PS concentrations, PS can partially react with the generated sulfate radicals (Eq. 2), which will reduce the quantity of oxidizing species and lower the BPA degradation efficiency [69]; (2) with respect to the higher PS concentration, the

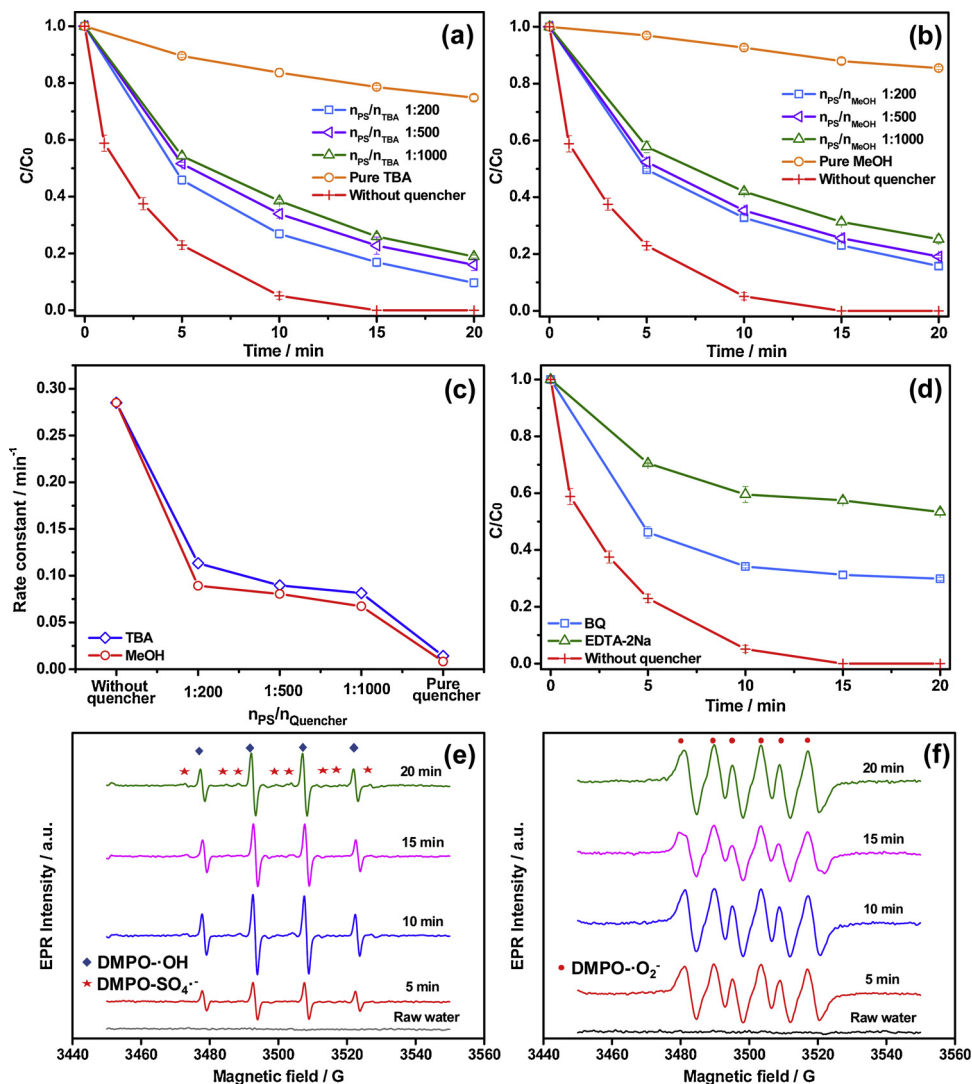
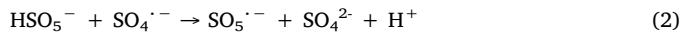


Fig. 7. (a) Effects of TBA on BPA degradation, (b) effects of MeOH on BPA degradation, (c) the rate constants at different molar ratios of scavengers relative to PS, (d) effects of BQ and EDTA-2Na on BPA degradation. EPR spectra of (e) the DMPO-SO₄^{•-} and DMPO-•OH adducts, and (f) the DMPO-•O₂⁻ adduct. (Photocatalyst: 50 mg; BPA: 10 mg/L, 100 mL; PS: 2 mM; and D35 dye solution: 17.84 μM for radical quenching experiments. DMPO concentration: 100 mM.)

photocatalyst dosage becomes a limiting factor, i.e., only part of the PS can be activated by the limited amount of catalyst in the system. Therefore, the BPA degradation efficiency is not greatly promoted as the PS concentration increases from 4 to 5 mM. Upon considering the dosage of the photocatalyst (0.5 g/L), we chose 2 mM as the PS concentration to realize cost-effectiveness.



3.4.5. Concentration of the D35 sensitizer

The concentration of the dye sensitizer is an important factor in dye-sensitized photocatalysis, which directly affects the photocatalytic performance. Therefore, it is of great significance to determine the appropriate D35 dye concentration in the sensitization process. In this study, 4 different dye concentrations, i.e., 8.92, 17.84, 35.68 and 71.36 μM , were investigated. As shown in Fig. 6e, 10 mg/L BPA is completely degraded within 20 min regardless of the dye concentration, and the degradation rate constants corresponding to the 4 dye concentrations are 0.208, 0.285, 0.400 and 0.461 min^{-1} , respectively. In particular, BPA can be eliminated within 15 or even 10 min when the D35 dye concentration increases from 17.84 to 71.36 μM . Therefore, it is obvious that the contaminant degradation rate and efficiency will be

promoted as the sensitizer concentration increases. We consider that this phenomenon is related to the light harvesting efficiency (LHE) of the dye-sensitized photocatalyst, which is similar to the mechanism of DSCs. The absorbance of dye sensitizers ($A(\lambda)$) is a significant parameter in the LHE, as expressed in the following Eq. 3:

$$\text{LHE} = 1 - 10^{-A(\lambda)} \quad (3)$$

$A(\lambda)$ is generally determined by factors such as the extinction coefficient, absorption range and dye loading [48,70]. Therefore, more sensitizers on the TiO₂ surface can absorb more incident visible-light photons to subsequently produce more electron-hole pairs. The photo-induced electrons can react with oxygen [71,72] and activate PS to generate several kinds of reactive oxidizing species [4], i.e., O₂^{•-}, •OH, and SO₄^{•-}. Additionally, the photo-induced holes on the sensitizers can also oxidize BPA. Thus, a higher D35 concentration will lead to more active oxidizing species being produced in the reaction system for a higher BPA degradation efficiency. Considering the balance between efficiency and economy, the D35 concentration of 17.84 μM was chosen in this study. More specifically, the amount of D35 anchored on the surface of TCN_{0.3} is calculated as about 0.66 mg D35/g TCN_{0.3} (details in SI, Section I).

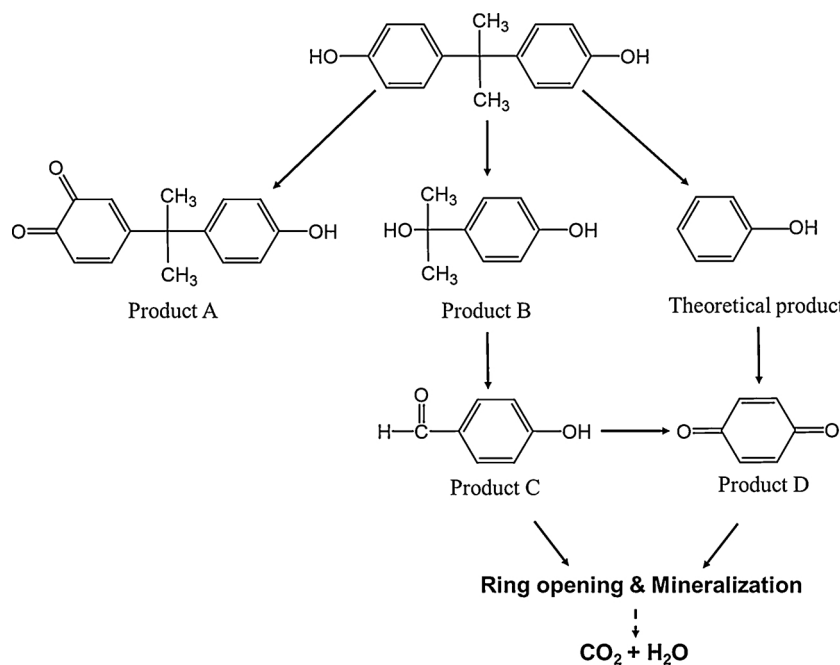


Fig. 8. Possible degradation pathways of BPA in the $\text{DTCN}_{0.3}/\text{PS}$ photocatalytic system.

3.5. Recyclability of the $\text{DTCN}_{0.3}$ photocatalyst

The recyclability of a photocatalyst is a very important factor in practical applications. The stability of $\text{DTCN}_{0.3}$ was investigated in 5 consecutive experiments involving PS activation for BPA degradation under visible light, as shown in Fig. 6f. In the 1st and 2nd cycles, BPA is almost completely degraded within 15 min. Moreover, 97%, 95% and 93% of BPA can be eliminated within 20 min in the next 3 cycles. Although the degradation efficiency slightly decreases over several cycles, the BPA removal process still remains fast and efficient. Furthermore, we also investigated the desorption of the D35 dye from the $\text{DTCN}_{0.3}$ photocatalyst by continuous stirring. 50 mg $\text{DTCN}_{0.3}$ powder was dispersed in 100 mL ultrapure water, and the TOC values of the water before and after 5 h of continuous stirring were measured. According to the results, the TOC value after the experiment (0.0673 mg/L) was almost unchanged compared with the initial value (0.05411 mg/L). Therefore, the D35 dye desorption from the $\text{DTCN}_{0.3}$ catalyst is negligible, which is in accordance with our previous study [29]. Thus, we believe that the as-prepared $\text{DTCN}_{0.3}$ has a good stability and recyclability to activate PS for contaminant degradation. In a future study, we will consider employing the $\text{DTCN}_{0.3}/\text{PS}$ photocatalytic system in a practical wastewater treatment process.

3.6. Identification of reactive oxidizing species

To explore the reaction mechanism of this $\text{DTCN}_{0.3}/\text{PS}$ photocatalytic system, it is necessary to examine the reactive oxidizing species in the BPA degradation process. Thus, radical quenching experiments were performed. Generally, there are two typical radicals in PS activation systems, i.e., $\text{SO}_4^{\cdot-}$ and 'OH [4]. In this study, we employed methanol (MeOH) and *tert*-butyl-alcohol (TBA) as two radical scavengers to evaluate the contributions of $\text{SO}_4^{\cdot-}$ and 'OH to the BPA degradation process. MeOH is an effective quencher for both $\text{SO}_4^{\cdot-}$ and 'OH , while TBA only scavenges 'OH [73,74]. We set different concentration gradients of the radical quenchers to observe the changes in BPA degradation. As shown in Fig. 7a, when TBA is added into the reaction system at different molar ratios relative to PS ($n[\text{TBA}/\text{PS}]$), including 200:1, 500:1 and 1000:1, the BPA degradation efficiency drops to 91%, 85% and 81%, respectively. When the aqueous solvent is

replaced by pure TBA, the BPA removal efficiency is only 25%. Similarly, when MeOH is added into the system, as observed with TBA, only 85%, 81%, 75% and 15% of the BPA can be eliminated within 20 min (Fig. 7b). The results show that the existence of TBA or MeOH markedly inhibits BPA degradation. Furthermore, compared with TBA, the increase of the MeOH concentration leads to a slightly faster decrease of the reaction rate (Fig. 7c), which indicates that the inhibiting effect of MeOH is stronger than that of TBA. Therefore, we infer that both $\text{SO}_4^{\cdot-}$ and 'OH are produced, and 'OH plays a more dominant role in the photocatalytic system. In addition to the contributions of $\text{SO}_4^{\cdot-}$ and 'OH , we also wondered whether $\text{'O}_2^{\cdot-}$ or h^+ (holes on $\text{g-C}_3\text{N}_4$ or D35 sensitizers) took part in the BPA degradation process. Thus, we respectively added 5 mM 1,4-benzoquinone (BQ, $\text{'O}_2^{\cdot-}$ scavenger) and EDTA-2Na (h^+ scavenger) into the reaction system (Fig. 7d) [75,76]. As expected, the BPA removal efficiency declined to some extent, which suggested that $\text{'O}_2^{\cdot-}$ and h^+ also participated in the BPA degradation.

To further confirm the existence of the mentioned reactive oxidizing species, electron spin resonance (EPR) spectroscopy was employed. DMPO acted as a spin-trapping agent to capture the produced radicals. $\text{SO}_4^{\cdot-}$ and 'OH are trapped in water solution, and $\text{'O}_2^{\cdot-}$ is probed in methanol medium [77]. As shown in Fig. 7e and f, no typical signal can be observed in darkness, either in water solution or in methanol medium. After visible-light illumination, the characteristic peaks of a mixture of DMPO- $\text{SO}_4^{\cdot-}$ and DMPO- 'OH adduct signals appear (Fig. 7e) [6]. In addition, the signal intensity of the DMPO- 'OH adduct is much stronger than the DMPO- $\text{SO}_4^{\cdot-}$ signal, which further verifies that the contribution of 'OH is larger than that of $\text{SO}_4^{\cdot-}$. This result is consistent with the results of the above radical trapping experiments. In addition, the DMPO- $\text{'O}_2^{\cdot-}$ adduct signal is also observed in methanol medium (Fig. 7f), which verifies the generation of $\text{'O}_2^{\cdot-}$ in the photocatalytic system. Therefore, it can be concluded that there are 4 types of reactive oxidizing species produced in the $\text{DTCN}_{0.3}/\text{PS}$ system, i.e., $\text{SO}_4^{\cdot-}$, 'OH , $\text{'O}_2^{\cdot-}$ and h^+ , having different levels of contribution to BPA removal.

3.7. Identification of products

The possible intermediate products formed during the BPA degradation process were investigated by LCMS-IT-TOF (Fig. S4). Four major intermediates were observed at specific reaction times, and their

possible molecular structures are displayed in Table S2. It is noteworthy that these intermediates have been detected in previous studies as well [29,40,78–81]. The possible pathways for BPA degradation in the $\text{DTCN}_{0.3}/\text{PS}$ photocatalytic system are proposed in Fig. 8. First, the electron-rich phenyl ring of BPA is attacked by $\cdot\text{OH}$ and SO_4^{2-} , and BPA is transformed into a cation after losing an electron from its aromatic ring. The produced BPA cation reacts with H_2O and is transformed into a more stable compound (product A). $\cdot\text{O}_2^-$ plays a significant role in the ring-cleavage of aromatic compounds [71]. After further oxidation, the ring-cleavage products 4-isopropanolphenol (product B) and phenol (in theoretical, but not detected) are formed [82]. Subsequently, 4-isopropanolphenol is converted into 4-hydroxybenzaldehyde (product C) through a dehydrogenation process, and phenol is converted into benzoquinone (product D) under dehydrogenation and hydroxylation processes [80]. Theoretically, 4-hydroxybenzaldehyde (product C) could also be directly transformed into benzoquinone (product D) through hydroxylation [80]. Furthermore, the intermediates are oxidized by SO_4^{2-} , $\cdot\text{OH}$, $\cdot\text{O}_2^-$ and h^+ upon undergoing dealkylation, decarboxylation and ring opening, generating small-molecule organics, such as oxalic acid, formic acid. Finally, these small molecules are mineralized into CO_2 and H_2O .

3.8. Degradation of various contaminants

Another 4 kinds of pollutants were tested to further explore the photocatalytic performance and selectivity of the $\text{DTCN}_{0.3}/\text{PS}$ system. We employed a 100 mL 10 mg/L water solution of methylene blue (MB), caffeine, acetaminophen (AAP) and phenol, which respectively represent dying, pharmaceutical and industrial wastewater. As displayed in Fig. 9, AAP can be completely degraded within 10 min, while MB and caffeine are eliminated in 30 min, with the addition of 0.5 g/L $\text{DTCN}_{0.3}$ and 2 mM PS. Although the degradation rate of phenol is lower than those of the former three contaminants, it can also be removed at nearly 80% within 60 min under the same reaction conditions. In principle, the photodegradability of organic pollutants highly depends on the following factors: their solubility in water, the electrostatic force between the photocatalysts and organics, and their molecular constitutions and electronic structures [83]. Although the electrostatic force may not be the dominant factor in this case with a neutral pH, it is worth noticing that phenol is much less soluble in water compared with the other compounds. This highly reduces the reactivity of radical oxidation processes. On the other hand, the molecular constitutions and electronic structures of these organics could play the most important role. The first three molecules (i.e., MB, caffeine and AAP) all have sp^3 hybrid orbitals (C–H bonds) and heteroatoms (e.g., N, S), which increases their degradability by oxygen radicals. More specifically, the

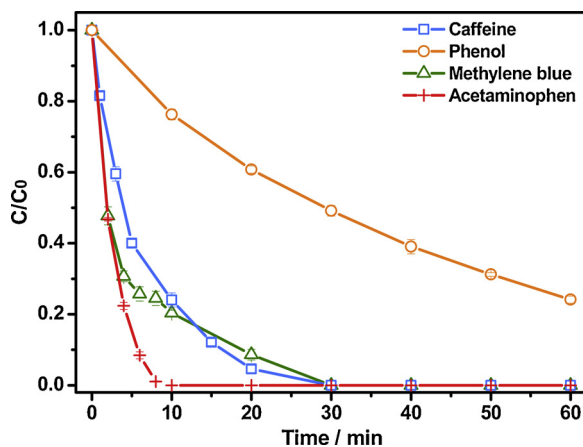


Fig. 9. Degradation efficiencies of various pollutants in the $\text{DTCN}_{0.3}/\text{PS}$ system under visible-light irradiation.

Table 1

The E_g , E_{VB} (E_{HOMO}) and E_{CB} (E_{LUMO}) of $\text{g-C}_3\text{N}_4$, TiO_2 and D35 dye.

Sample	E_g (eV) (E_{HOMO} for D35)	E_{VB} (eV) (E_{HOMO} for D35)	E_{CB} (eV) (E_{LUMO} for D35)
$\text{g-C}_3\text{N}_4$	2.69	1.79	-0.9
TiO_2	3.18	2.43	-0.75
D35 dye	2.41	1.04	-1.37

methyl groups in MB tend to be first oxidized via H-abstraction leading to demethylation, and the C–H bond on the carbon between two imidazole nitrogen atoms in caffeine could be readily oxidized by radicals [84,85], while the most electron-rich AAP could be easily oxidized into quinone derivatives [86]. In contrast, the molecular structure of phenol is relatively more stable than those of the others, with the delocalized π_7^8 bond leading to its lower degradability. In short, these results indicate that the $\text{DTCN}_{0.3}/\text{PS}$ system exhibits a highly efficient photocatalytic performance and non-selectivity for the visible-light-driven photodegradation of various organic contaminants. Therefore, it has great potential to be applied in practical wastewater treatment processes in the future.

3.9. Mechanism of the $\text{DTCN}_{0.3}/\text{PS}$ system

As discussed in Section 3.1.5, due to the appropriate energy level alignment of D35, $\text{g-C}_3\text{N}_4$ and TiO_2 (Table 1), the $\text{D35-TiO}_2/\text{g-C}_3\text{N}_4$ photocatalyst is feasible as designed. As shown in the UV-vis spectra, the light absorption boundary of $\text{g-C}_3\text{N}_4$ is approximately 450 nm and that of TiO_2 is approximately 390 nm. When the TCN composite is illuminated by visible light ($\lambda > 400$ nm), only $\text{g-C}_3\text{N}_4$ can be excited, i.e., the electrons are injected into its conduction band ($e_{\text{C}_3\text{N}_4}$), leaving holes ($h_{\text{C}_3\text{N}_4}^+$) in its valence band. The CB edge of $\text{g-C}_3\text{N}_4$ is higher than that of TiO_2 , and such an appropriate energy level difference provides sufficient driving force for the electron injection from $\text{g-C}_3\text{N}_4$ CB into TiO_2 CB, which therefore enhances the charge separation efficiency [37,87–89]. After dye-sensitization, the D35 dye anchors onto the TiO_2 surface via its carboxylic group, forming a bidentate chemical bond [33,48]. The wide visible-light absorption of D35 dye (400–675 nm) fitly complements the absorption of $\text{TiO}_2/\text{g-C}_3\text{N}_4$ (< 450 nm) leading to almost full-visible-spectrum light harvesting. Upon visible-light excitation, the electrons in D35 HOMO are excited into the LUMO, and are then injected into the TiO_2 CB due to the matching energy level difference [29,33,48,90], which also effectively improves the charge-carrier separation. Hence, the complementary light absorption ranges of TCN and D35 dye endow $\text{DTCN}_{0.3}$ with remarkably high visible-light harvesting ability, meanwhile the desirable energy level alignment greatly enhances the charge-carrier separation.

According to the above analysis, a feasible mechanism of the $\text{DTCN}_{0.3}/\text{PS}$ photocatalytic system is proposed (Fig. 10). When $\text{DTCN}_{0.3}$ is illuminated by visible light, both $\text{g-C}_3\text{N}_4$ (Eq. 4) and D35 (Eq. 5) are simultaneously excited and inject electrons into TiO_2 CB. On one hand, the free electrons react with the electrophilic oxygen of persulfate leading to homolytic cleavage of the O–O bond to generate sulfate radicals (Eq. 6) [91]. Moreover, part of the produced SO_4^{2-} can further oxidize H_2O to generate $\cdot\text{OH}$ (Eq. 7) [92]. On the other hand, the energy level of the TiO_2 CB is much more negative than the reduction potential of oxygen ($E_{\text{O}_2/\text{O}_2^-}^0 = -0.046$ eV, vs. NHE) [93]; thus, some of the free electrons in TiO_2 CB can react with the O_2^- adsorbed onto the TiO_2 surface to produce $\cdot\text{O}_2^-$ (Eq. 8), further generating $\cdot\text{OH}$ (Eq. 9) [71,72]. As a result, the formed reactive oxidizing species, i.e., SO_4^{2-} , $\cdot\text{O}_2^-$ and $\cdot\text{OH}$, lead to the oxidative degradation of contaminants (Eq. 10). Additionally, after electron injection, holes (h^+) are left on the $\text{g-C}_3\text{N}_4$ VB and D35 HOMO. Unfortunately, neither of the holes can oxidize H_2O ($E_{\text{OH}/\text{H}_2\text{O}}^0 = 2.68$ eV, vs. NHE) or OH^- ($E_{\text{OH}/\text{OH}^-}^0 = 1.99$ eV, vs. NHE) to produce $\cdot\text{OH}$ [94], as the energy levels of both the $\text{g-C}_3\text{N}_4$

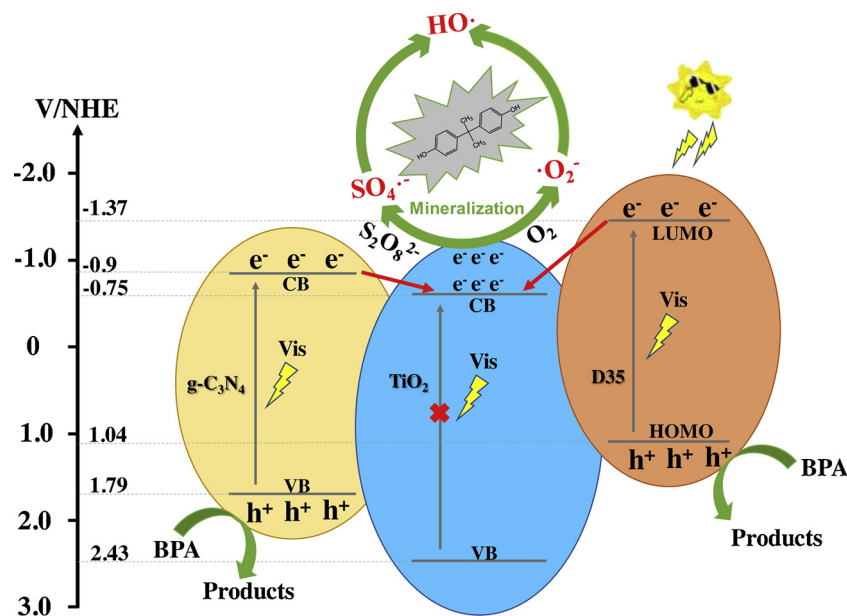
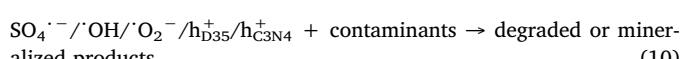
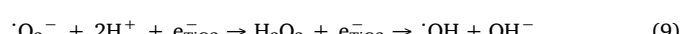
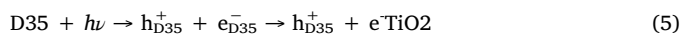


Fig. 10. Mechanism of contaminant degradation in the $\text{DTCN}_{0.3}/\text{PS}$ photocatalytic system under visible-light irradiation.

VB and the D35 HOMO are much higher (less positive). However, the holes can directly oxidize the contaminants (Eq. 10). Furthermore, when the holes on the D35 HOMO oxidize organic contaminants, the oxidized D35 dye (state after electron injection) can be regenerated (Eq. 11), so that the catalysts can be reused in the next photocatalytic cycle [29].

In short, $\text{g-C}_3\text{N}_4$ and D35 have complementary visible-light absorption ranges for $\text{DTCN}_{0.3}$. Moreover, the electrons injected into the TiO_2 CB from both components synergistically activate persulfate to produce reactive oxidizing species for contaminants photodegradation. The electron transfer processes in the $\text{DTCN}_{0.3}/\text{PS}$ photocatalytic system are summarized as follows:



4. Conclusion

$\text{g-C}_3\text{N}_4$ is successfully combined with TiO_2 by the hydrothermal method, which enhances the charge-carrier separation efficiency. To further improve the photocatalytic performance, D35 dye is anchored onto TiO_2 to broaden the visible-light absorption range. Thus, more free electrons can be generated by the $\text{DTCN}_{0.3}$ nanocomposites for more efficient PS activation and reactive oxidizing species production to eliminate organic pollutants. Under the optimum experimental conditions, a 100 mL BPA solution (10 mg/L) can be degraded within 15 min, and nearly 50% of the BPA is mineralized. There are 4 kinds of reactive oxidizing species identified during BPA elimination, i.e., $\text{SO}_4^{\cdot-}$, $\cdot\text{OH}$, $\cdot\text{O}_2^-$ and h^+ , and $\cdot\text{OH}$ plays a more important role than $\text{SO}_4^{\cdot-}$. In addition to the high degradation efficiency of BPA, the $\text{DTCN}_{0.3}/\text{PS}$

photocatalytic system also shows efficient performance in eliminating organic pollutants in dyeing, pharmaceutical and industrial wastewater without selectivity. Furthermore, the $\text{DTCN}_{0.3}$ photocatalyst has relatively high stability and recyclability. Therefore, the $\text{D35-TiO}_2/\text{g-C}_3\text{N}_4/\text{PS}$ photocatalytic system provides a promising pathway to degrade micropollutants in wastewater.

Conflicts of interest

There are no conflicts to declare.

Acknowledgement

This study was financially supported by the National Key Research and Development Project (Grant NO. 2016YFC0400701), the Program for Innovative Research Team in Shaanxi (Grant No. 2013KCT-13), the National Natural Science Foundation of China (51808434), the Natural Science Basic Research Plan in Shaanxi Province of China (Program No.2018JQ5129), the Scientific Research Program Funded by Shaanxi Provincial Education Department (Program No.18JK0455), and the Chinese Government “Hundred Talent Program of Shaanxi Provence”.

Appendix A. Supplementary data

Supplementary material related to this article can be found, in the online version, at doi:<https://doi.org/10.1016/j.apcatb.2019.117759>.

References

- [1] A.N. Gounden, S. Singh, S.B. Jonnalagadda, Simultaneous removal of 2,4,6-tribromophenol from water and bromate ion minimization by ozonation, *J. Hazard. Mater.* 357 (2018) 415–423.
- [2] X. Liu, Y. Zhou, J. Zhang, L. Luo, Y. Yang, H. Huang, H. Peng, L. Tang, Y. Mu, Insight into electro-Fenton and photo-Fenton for the degradation of antibiotics: mechanism study and research gaps, *Chem. Eng. J.* 347 (2018) 379–397.
- [3] C. Byrne, G. Subramanian, S.C. Pillai, Recent advances in photocatalysis for environmental applications, *J. Environ. Chem. Eng.* 6 (2018) 3531–3555.
- [4] J. Wang, S. Wang, Activation of persulfate (PS) and peroxymonosulfate (PMS) and application for the degradation of emerging contaminants, *Chem. Eng. J.* 334 (2018) 1502–1517.
- [5] M. Wei, L. Gao, J. Li, J. Fang, W. Cai, X. Li, A. Xu, Activation of peroxymonosulfate by graphitic carbon nitride loaded on activated carbon for organic pollutants degradation, *J. Hazard. Mater.* 316 (2016) 60–68.
- [6] C. Qi, G. Yu, J. Huang, B. Wang, Y. Wang, S. Deng, Activation of persulfate by modified drinking water treatment residuals for sulfamethoxazole degradation,

Chem. Eng. J. 353 (2018) 490–498.

[7] S. Yang, X. Qiu, P. Jin, M. Dzakpasu, X.C. Wang, Q. Zhang, L. Zhang, L. Yang, D. Ding, W. Wang, K. Wu, MOF-templated synthesis of CoFe_2O_4 nanocrystals and its coupling with peroxyomonosulfate for degradation of bisphenol A, *Chem. Eng. J.* 353 (2018) 329–339.

[8] N. Zrinyi, A.L. Pham, Oxidation of benzoic acid by heat-activated persulfate: effect of temperature on transformation pathway and product distribution, *Water Res.* 120 (2017) 43.

[9] M.G. Antoniou, A.A.D.L. Cruz, D.D. Dionysiou, Degradation of microcystin-LR using sulfate radicals generated through photolysis, thermolysis and e^- transfer mechanisms, *Appl. Catal. B-Environ.* 96 (2010) 290–298.

[10] P. Xu, N.S. McCool, T.E. Mallouk, Water splitting dye-sensitized solar cells, *Nano Today* (2017) S1748013217300087.

[11] Z. Wei, F.A. Villamena, L.K. Weavers, Kinetics and mechanism of ultrasonic activation of persulfate: an in-situ EPR spin trapping study, *Environ. Sci. Technol.* 51 (2017).

[12] A. Rastogi, S.R. Al-Abed, D.D. Dionysiou, Sulfate radical-based ferrous-peroxymonosulfate oxidative system for PCBs degradation in aqueous and sediment systems, *Appl. Catal. B-Environ.* 85 (2009) 171–179.

[13] G.P. Anipsitakis, D.D. Dionysiou, Degradation of organic contaminants in water with sulfate radicals generated by the conjunction of peroxyomonosulfate with cobalt, *Environ. Sci. Technol.* 37 (2003) 4790.

[14] X. Duan, H. Sun, J. Kang, Y. Wang, S. Indrawirawan, S. Wang, Insights into heterogeneous catalysis of persulfate activation on dimensional-structured nanocarbons, *ACS Catal.* 5 (2015) 4629–4636.

[15] A. Thomas, A. Fischer, F. Goettmann, M. Antonietti, J.O. Muller, R. Schlogl, J.M. Carlsson, Graphitic carbon nitride materials: variation of structure and morphology and their use as metal-free catalysts, *J. Mater. Chem.* 18 (2008) 4893–4908.

[16] P. Zhang, X. Li, C. Shao, Y. Liu, Hydrothermal synthesis of carbon-rich graphitic carbon nitride nanosheets for photoredox catalysis, *J. Mater. Chem. 3* (2015) 3281–3284.

[17] D. Masih, Y. Ma, S. Rohani, Graphitic C_3N_4 based noble-metal-free photocatalyst systems: a review, *Appl. Catal. B-Environ.* 206 (2017) 556–588.

[18] X. Bai, L. Wang, Y. Wang, W. Yao, Y. Zhu, Enhanced oxidation ability of g- C_3N_4 photocatalyst via C60 modification, *Appl. Catal. B-Environ.* 152–153 (2014) 262–270.

[19] B. Liu, M. Qiao, Y. Wang, L. Wang, Y. Gong, T. Guo, X. Zhao, Persulfate enhanced photocatalytic degradation of bisphenol A by g- C_3N_4 nanosheets under visible light irradiation, *Chemosphere* 189 (2017) 115–122.

[20] Y. Feng, C. Liao, L. Kong, D. Wu, Y. Liu, P.H. Lee, K. Shih, Facile synthesis of highly reactive and stable Fe-doped g- C_3N_4 composites for peroxyomonosulfate activation: a novel nonradical oxidation process, *J. Hazard. Mater.* 354 (2018) 63–71.

[21] J.G. Kim, S.M. Park, M.E. Lee, E.E. Kwon, K. Baek, Photocatalytic co-oxidation of As (III) and Orange G using urea-derived g- C_3N_4 and persulfate, *Chemosphere* 212 (2018) 193–199.

[22] H. Tang, S. Chang, L. Jiang, G. Tang, W. Liang, Novel spindle-shaped nanoporous TiO_2 coupled graphitic g- C_3N_4 nanosheets with enhanced visible-light photocatalytic activity, *Ceram. Int.* 391 (2016).

[23] C. Li, Z. Sun, Y. Xue, G. Yao, S. Zheng, A facile synthesis of g- C_3N_4 /TiO₂ hybrid photocatalysts by sol-gel method and its enhanced photodegradation towards methylene blue under visible light, *Adv. Powder Technol.* 27 (2016) 330–337.

[24] S.T. Martin, M.R. Hoffmann, W. Choi, D.W. Bahnemann, Environmental applications of semiconductor photocatalysis, *Chem. Rev.* 95 (1995) 69–96.

[25] R. Vinu, S. Polisetti, G. Madras, Dye sensitized visible light degradation of phenolic compounds, *Chem. Eng. J.* 165 (2010) 784–797.

[26] J.S. Miller, Rose bengal-sensitized photooxidation of 2-chlorophenol in water using solar simulated light, *Water Res.* 39 (2005) 412–422.

[27] D. Chatterjee, A. Mahata, Visible light induced photodegradation of organic pollutants on dye adsorbed TiO_2 surface, *J. Photochem. Photobiol. A: Chem.* 153 (2002) 199–204.

[28] D. Chatterjee, A. Mahata, Demineralization of organic pollutants on the dye modified TiO_2 semiconductor particulate system using visible light, *Appl. Catal. B-Environ.* 33 (2001) 119–125.

[29] X. Bai, L. Yang, A. Hagfeldt, E.M.J. Johansson, P. Jin, D35-TiO₂ nano-crystalline film as a high performance visible-light photocatalyst towards the degradation of bis-phenol A, *Chem. Eng. J.* 355 (2019) 999–1010.

[30] C. Chen, W. Ma, J. Zhao, ChemInform abstract: semiconductor-mediated photodegradation of pollutants under visible-light irradiation, *Chem. Soc. Rev.* 42 (2011) 4206.

[31] S. Afzal, W.A. Daoud, S.J. Langford, Photostable self-cleaning cotton by a copper (II) porphyrin/TiO₂ visible-light photocatalytic system, *ACS Appl. Mater. & Inter.* 5 (2013) 4753–4759.

[32] L.M. Peter, The Grätzel, Cell: where next? *J. Phys. Chem. Lett.* 2 (2011) 1861–1867.

[33] Z. Youssef, L. Colombeau, N. Yesmurzayeva, F. Baros, R. Vanderesse, T. Hamieh, J. Toufaïly, C. Frochot, T. Roques-Carmes, S. Acherrar, Dye-sensitized nanoparticles for heterogeneous photocatalysis: Cases studies with TiO_2 , ZnO , fullerene and graphene for water purification, *Dye. Pigment.* 159 (2018) 49–71.

[34] S.M. Feldt, E.A. Gibson, G. Erik, S. Licheng, B. Gerrit, H. Anders, Design of organic dyes and cobalt polypyridine redox mediators for high-efficiency dye-sensitized solar cells, *J. Am. Chem. Soc.* 132 (2010) 16714–16724.

[35] E. Gabrielsson, H. Ellis, S. Feldt, H. Tian, G. Boschloo, A. Hagfeldt, L. Sun, Convergent/divergent synthesis of a linker-varied series of dyes for dye-sensitized solar cells based on the D35 donor, *Adv. Energy Mater.* 3 (2013) 1647–1656.

[36] D.P. Hagberg, X. Jiang, E. Gabrielsson, M. Linder, T. Marinado, T. Brinck, A. Hagfeldt, L. Sun, Symmetric and unsymmetric donor functionalization comparing structural and spectral benefits of chromophores for dye-sensitized solar cells, *J. Mater. Chem.* 19 (2009) 7232.

[37] R. Hao, G. Wang, H. Tang, L. Sun, C. Xu, D. Han, Template-free preparation of macro/mesoporous g- C_3N_4 /TiO₂ heterojunction photocatalysts with enhanced visible light photocatalytic activity, *Appl. Catal. B-Environ.* 187 (2016) 47–58.

[38] W. Zhen, F. Liang, Y. Liu, W. Luo, Y. Zhu, Photoelectrocatalytic degradation of phenol-containing wastewater by TiO₂/g- C_3N_4 hybrid heterostructure thin film, *Appl. Catal. B-Environ.* 201 (2017) 600–606.

[39] S. Ardo, G.J. Meyer, Photodriven heterogeneous charge transfer with transition-metal compounds anchored to TiO₂ semiconductor surfaces, *Chem. Soc. Rev.* 38 (2009) 115–164.

[40] B. Darsinou, Z. Frontistis, M. Antonopoulou, I. Konstantinou, D. Mantzavinos, Sonication-activated persulfate oxidation of bisphenol A: kinetics, pathways and the controversial role of temperature, *Chem. Eng. J.* 280 (2015) 623–633.

[41] Z. Wei, F. Liang, Y. Liu, W. Luo, J. Wang, W. Yao, Y. Zhu, Photoelectrocatalytic degradation of phenol-containing wastewater by TiO₂/g- C_3N_4 hybrid heterostructure thin film, *Appl. Catal. B-Environ.* 201 (2017) 600–606.

[42] G. Zhang, T. Zhang, B. Li, S. Jiang, X. Zhang, L. Hai, X. Chen, W. Wu, An ingenious strategy of preparing TiO₂/g- C_3N_4 heterojunction photocatalyst: In situ growth of TiO₂ nanocrystals on g- C_3N_4 nanosheets via impregnation-calcination method, *Appl. Surf. Sci.* 433 (2018) 963–974.

[43] Y. Tan, Z. Shu, J. Zhou, T. Li, W. Wang, Z. Zhao, One-step synthesis of nanostructured g- C_3N_4 /TiO₂ composite for highly enhanced visible-light photocatalytic H_2 evolution, *Appl. Catal. B-Environ.* 230 (2018) 260–268.

[44] Z. Lu, L. Zeng, W. Song, Z. Qin, D. Zeng, C. Xie, In situ synthesis of C-TiO₂/g- C_3N_4 heterojunction nanocomposite as highly visible light active photocatalyst originated from effective interfacial charge transfer, *Appl. Catal. B-Environ.* 202 (2017) 489–499.

[45] S. Tan, Z. Xing, J. Zhang, Z. Li, X. Wu, J. Cui, J. Kuang, Q. Zhu, W. Zhou, Ti^{3+} - TiO_2 /g- C_3N_4 mesostructured nanosheets heterojunctions as efficient visible-light-driven photocatalysts, *J. Catal.* 357 (2018) 90–99.

[46] X. Wang, F. Wang, C. Bo, K. Cheng, J. Wang, J. Zhang, H. Song, Promotion of phenol photodecomposition and the corresponding decomposition mechanism over TiO₂/g- C_3N_4 nanocomposites, *Appl. Surf. Sci.* 453 (2018) 320–329.

[47] C. Díaz-Uribe, W. Vallejo, K. Campos, W. Solano, J. Andrade, A. Muñoz-Acevedo, E. Schott, X. Zarate, Improvement of the photocatalytic activity of TiO₂ using Colombian Caribbean species (*Syzygium cumini*) as natural sensitizers: experimental and theoretical studies, *Dye. Pigment.* 150 (2018) 370–376.

[48] A. Hagfeldt, G. Boschloo, L. Sun, L. Kloo, H. Pettersson, Dye-sensitized solar cells, *Chem. Rev.* 110 (2010) 6595.

[49] T.J. Meyer, G.J. Meyer, B.W. Pfennig, J.R. Schoonover, B.M. Peek, Molecular-level electron transfer and excited state assemblies on surfaces of metal oxides and glass, *Inorg. Chem.* 33 (1994) 3952–3964.

[50] K. Murakoshi, G. Kano, Y. Wada, S. Yanagida, H. Miyazaki, M. Matsumoto, S. Murasawa, Importance of binding states between photosensitizing molecules and the TiO₂ surface for efficiency in a dye-sensitized solar cell, *J. Electroanal. Chem.* Lausanne (Lausanne) 396 (1995) 27–34.

[51] G. Xin, Y. Meng, Pyrolysis synthesized g- C_3N_4 for photocatalytic degradation of methylene blue, *J. Chem-NY.* 2013 (2013) 1–5.

[52] X. Gao, S. Li, T. Li, G. Li, H. Ma, g- C_3N_4 as a saturable absorber for the passively Q-switched Nd:YLF laser at 13 μm , *Photonics. Res.* 5 (2017) 33.

[53] X. Ma, Y. Wei, Z. Wei, H. He, C. Huang, Y. Zhu, Probing pi-pi stacking modulation of g- C_3N_4 /graphene heterojunctions and corresponding role of graphene on photocatalytic activity, *J. Colloid Interface Sci.* 508 (2017) 274–281.

[54] A. Zada, Y. Qu, S. Ali, N. Sun, H. Lu, R. Yan, X. Zhang, L. Jing, Improved visible-light activities for degrading pollutants on TiO₂/g- C_3N_4 nanocomposites by decorating SPR Au nanoparticles and 2,4-dichlorophenol decomposition path, *J. Hazard. Mater.* 342 (2017) 715–723.

[55] E. Palomares, J.N. Clifford, S.A. Haque, A.T. Lutz, J.R. Durrant, Control of charge recombination dynamics in dye sensitized solar cells by the use of conformally deposited metal oxide blocking layers, *J. Am. Chem. Soc.* 125 (2016) 475–482.

[56] Q. Jiang, L. Zhang, H. Wang, X. Yang, J. Meng, H. Liu, Z. Yin, J. Wu, X. Zhang, J. You, Enhanced electron extraction using SnO₂ for high-efficiency planar-structure HC(NH₂)₂PbI₃⁻ based perovskite solar cells, *Nat. Energy* 2 (2016).

[57] L. Xu, L. Yang, E.M.J. Johansson, Y. Wang, P. Jin, Photocatalytic activity and mechanism of bisphenol A removal over TiO_{2-x}/rGO nanocomposite driven by visible light, *Chem. Eng. J.* 350 (2018) 1043–1055.

[58] X. Song, Y. Hu, M. Zheng, C. Wei, Solvent-free in situ synthesis of g- C_3N_4 / TiO_2 composite with enhanced UV- and visible-light photocatalytic activity for NO oxidation, *Appl. Catal. B-Environ.* 182 (2016) 587–597.

[59] K. Sridharan, E. Jang, T.J. Park, Novel visible light active graphitic g- C_3N_4 -TiO₂ composite photocatalyst: synergistic synthesis, growth and photocatalytic treatment of hazardous pollutants, *Appl. Catal. B-Environ.* 142–143 (2013) 718–728.

[60] S. Zhou, Y. Liu, J. Li, Y. Wang, G. Jiang, Z. Zhao, D. Wang, A. Duan, J. Liu, X. Wei, Facile in situ synthesis of graphitic carbon nitride (g- C_3N_4)-N-TiO₂ heterojunction as an efficient photocatalyst for the selective photoreduction of CO₂ to CO, *Appl. Catal. B-Environ.* 158–159 (2014) 20–29.

[61] K.E. Lee, M.A. Gomez, T. Regier, Y. Hu, G.P. Demopoulos, Further understanding of the electronic interactions between N719 sensitizer and anatase TiO₂ films: a combined x-ray absorption and x-ray photoelectron spectroscopic study, *J. Phys. Chem. C* 115 (2011) 5692–5707.

[62] J. Singh, A. Gusain, V. Saxena, A.K. Chauhan, P. Veerender, S.P. Koiry, P. Jha, A. Jain, D.K. Aswal, S.K. Gupta, U.V.-Vis XPS, FTIR, and EXAFS studies to investigate the binding mechanism of N719 dye onto oxalic acid treated TiO₂ and its implication on photovoltaic properties, *J. Phys. Chem. C* 117 (2013) 21096–21104.

[63] L. Tang, Y. Liu, J. Wang, G. Zeng, Y. Deng, H. Dong, H. Feng, J. Wang, B. Peng,

Enhanced activation process of persulfate by mesoporous carbon for degradation of aqueous organic pollutants: electron transfer mechanism, *Appl. Catal. B-Environ.* 231 (2018) 1–10.

[64] R.A. Doong, C.Y. Liao, Enhanced visible-light-responsive photodegradation of bisphenol A by Cu, N-codoped titanate nanotubes prepared by microwave-assisted hydrothermal method, *J. Hazard. Mater.* 322 (2017) 254–262.

[65] X. Xiao, R. Hao, X. Zuo, J. Nan, L. Li, W. Zhang, Microwave-assisted synthesis of hierarchical $\text{Bi}_2\text{O}_3\text{I}_3$ microsheets for efficient photocatalytic degradation of bisphenol-A under visible light irradiation, *Chem. Eng. J.* 209 (2012) 293–300.

[66] N. Lu, Y. Lu, F. Liu, K. Zhao, X. Yuan, Y. Zhao, Y. Li, H. Qin, J. Zhu, $\text{H}_3\text{PW}_{12}\text{O}_{40}/\text{TiO}_2$ catalyst-induced photodegradation of bisphenol A (BPA): kinetics, toxicity and degradation pathways, *Chemosphere* 91 (2013) 1266–1272.

[67] B. Gao, T.M. Lim, D.P. Subagio, T.T. Lim, Zr -doped TiO_2 for enhanced photocatalytic degradation of bisphenol A, *Appl. Catal. B-Environ.* 375 (2010) 107–115.

[68] S.B. Hammouda, F. Zhao, Z. Safaei, D.L. Ramasamy, B. Doshi, M. Sillanpää, Sulfate radical-mediated degradation and mineralization of bisphenol F in neutral medium by the novel magnetic $\text{Sr}_2\text{CoFeO}_6$ double perovskite oxide catalyzed peroxymonosulfate: Influence of co-existing chemicals and UV irradiation, *Appl. Catal. B-Environ.* 233 (2018) 99–111.

[69] A. Al-Anazi, W.H. Abdelraheem, C. Han, M.N. Nadagouda, L. Sygellou, M.K. Arfanis, P. Falaras, V.K. Sharma, D.D. Dionysiou, Cobalt ferrite nanoparticles with controlled composition-peroxymonosulfate mediated degradation of 2-phenylbenzimidazole-5-sulfonic acid, *Appl. Catal. B-Environ.* 221 (2018).

[70] L. Yang, Hole Transport Materials for Solid-state Mesoscopic Solar Cells, Uppsala University, 2014.

[71] J. Ng, X. Wang, D.D. Sun, One-pot hydrothermal synthesis of a hierarchical nano-fungus-like anatase TiO_2 thin film for photocatalytic oxidation of bisphenol A, *Appl. Catal. B-Environ.* 110 (2011) 260–272.

[72] D.P. Subagio, M. Srinivasan, M. Lim, T.T. Lim, Photocatalytic degradation of bisphenol-A by nitrogen-doped TiO_2 hollow sphere in a vis-LED photoreactor, *Appl. Catal. B-Environ.* 95 (2010) 414–422.

[73] P. Neta, R.E. Huie, A.B. Ross, Rate Constants for Reactions of Inorganic Radicals in Aqueous Solution, Dept. of Commerce, U. S, 1979.

[74] G.V. Buxton, C.L. Greenstock, W.P. Helman, A.B. Ross, Critical review of rate constants for reactions of hydrated electrons, hydrogen atoms and hydroxyl radicals (OH/O^\cdot) in aqueous solution, *J. Phys. Chem. Ref. Data* 17 (1988) 513–886.

[75] X. Yang, J. Qin, Y. Jiang, K. Chen, X. Yan, D. Zhang, R. Li, H. Tang, Fabrication of $\text{P25}/\text{Ag}_3\text{PO}_4$ /graphene oxide heterostructures for enhanced solar photocatalytic degradation of organic pollutants and bacteria, *Appl. Catal. B-Environ.* 166–167 (2015) 231–240.

[76] H. Tang, S. Chang, K. Wu, G. Tang, Y. Fu, Q. Liu, X. Yang, Band gap and morphology engineering of TiO_2 by silica and fluorine co-doping for efficient ultraviolet and visible photocatalysis, *RSC Adv.* 6 (2016) 63117–63130.

[77] Y. Zhu, Y. Wang, Z. Chen, L. Qin, L. Yang, L. Zhu, P. Tang, T. Gao, Y. Huang, Z. Sha, Visible light induced photocatalysis on CdS quantum dots decorated TiO_2 nanotube arrays, *Appl. Catal. A-Gen.* 498 (2015) 159–166.

[78] D.P. Subagio, M. Srinivasan, M. Lim, T.T. Lim, Photocatalytic degradation of bisphenol-A by nitrogen-doped TiO_2 hollow sphere in a vis-LED photoreactor, *Appl. Catal. B-Environ.* 95 (2010) 414–422.

[79] V. Repousi, A. Petala, Z. Frontistis, M. Antonopoulou, I. Konstantinou, D.I. Kondarides, D. Mantzavinos, Photocatalytic degradation of bisphenol A over Rh/TiO_2 suspensions in different water matrices, *Catal. Today* 284 (2017) 59–66.

[80] Z.H. Diao, Q. Wei, P.R. Guo, L.J. Kong, S.Y. Pu, Photo-assisted degradation of bisphenol A by a novel $\text{Fe}_2\text{S}_2@\text{SiO}_2$ microspheres activated persulfate process: synergistic effect, pathway and mechanism, *Chem. Eng. J.* 349 (2018) 683–693.

[81] Y.G. Kang, H.C. Vu, T.T. Le, Y.S. Chang, Activation of persulfate by a novel $\text{Fe}(\text{II})$ -immobilized chitosan/alginate composite for bisphenol A degradation, *Chem. Eng. J.* 353 (2018) 736–745.

[82] L. Wen, P.X. Wu, Y. Zhu, Z.J. Huang, Y.H. Lu, Y.W. Li, D. Zhi, N.W. Zhu, Catalytic degradation of bisphenol A by CoMnAl mixed metal oxides catalyzed peroxymonosulfate: performance and mechanism, *Chem. Eng. J.* 279 (2015) 93–102.

[83] L. Yang, L. Xu, X. Bai, P. Jin, Enhanced visible-light activation of persulfate by Ti^{3+} self-doped TiO_2 /graphene nanocomposite for the rapid and efficient degradation of micropollutants in water, *J. Hazard. Mater.* 365 (2019) 107–117.

[84] L. Wolski, M. Ziolek, Insight into pathways of methylene blue degradation with H_2O_2 over mono and bimetallic Nb , Zn oxides, *Appl. Catal. B-Environ.* 224 (2018) 634–647.

[85] F. Qi, W. Chu, B. Xu, Catalytic degradation of caffeine in aqueous solutions by cobalt-MCM41 activation of peroxymonosulfate, *Appl. Catal. B-Environ.* 134–135 (2013) 324–332.

[86] B. Yang, G.G. Ying, J.L. Zhao, S. Liu, L.J. Zhou, F. Chen, Removal of selected endocrine disrupting chemicals (EDCs) and pharmaceuticals and personal care products (PPCPs) during ferrate (VI) treatment of secondary wastewater effluents, *Water Res.* 46 (2012) 2194–2204.

[87] Y. Yang, Y. Guo, F. Liu, Y. Xing, Y. Guo, S. Zhang, G. Wan, M. Huo, Preparation and enhanced visible-light photocatalytic activity of silver deposited graphitic carbon nitride plasmonic photocatalyst, *Appl. Catal. B-Environ.* 142 (2013) 828–837.

[88] Y. Wang, W. Yang, X. Chen, J. Wang, Y. Zhu, Photocatalytic activity enhancement of core-shell structure $\text{g-C}_3\text{N}_4@\text{TiO}_2$ via controlled ultrathin $\text{g-C}_3\text{N}_4$ layer, *Appl. Catal. B-Environ.* 220 (2018) 337–347.

[89] Y.N. Li, Z.Y. Chen, M.Q. Wang, L.Z. Zhang, S.J. Bao, Interface engineered construction of porous $\text{g-C}_3\text{N}_4/\text{TiO}_2$ heterostructure for enhanced photocatalysis of organic pollutants, *Appl. Surf. Sci.* 440 (2018) 229–236.

[90] C. Chen, W. Ma, J. Zhao, Semiconductor-mediated photodegradation of pollutants under visible-light irradiation, *Chem. Soc. Rev.* 39 (2010) 4206–4219.

[91] Y. Guo, Z. Zeng, Y. Zhu, Z. Huang, Y. Cui, J. Yang, Catalytic oxidation of aqueous organic contaminants by persulfate activated with sulfur-doped hierarchically porous carbon derived from thiophene, *Appl. Catal. B-Environ.* 220 (2018) 635–644.

[92] Y. Liu, H. Guo, Y. Zhang, X. Cheng, P. Zhou, G. Zhang, J. Wang, P. Tang, T. Ke, W. Li, Heterogeneous activation of persulfate for Rhodamine B degradation with 3D flower sphere-like $\text{BiOI}/\text{Fe}_3\text{O}_4$ microspheres under visible light irradiation, *Sep. Purif. Technol.* 192 (2018) 88–98.

[93] C. Bo, T. Peng, M. Jing, L. Kan, Z. Ling, Graphitic carbon nitride ($\text{g-C}_3\text{N}_4$)- Pt-TiO_2 nanocomposite as an efficient photocatalyst for hydrogen production under visible light irradiation, *Phys. Chem. Chem. Phys.* 14 (2012) 16745–16752.

[94] Y. He, L. Zhang, B. Teng, M. Fan, New application of Z-scheme $\text{Ag}_3\text{PO}_4/\text{g-C}_3\text{N}_4$ composite in converting CO_2 to fuel, *Environ. Sci. Technol.* 49 (2015) 649–656.